Spectroscopic Analysis of Samples in Aqueous Environments using a Hollow Core Fiber

by

Akshara Adike
B.Tech, Sri Padmavati Mahila Visvavidyalayam, 2012

A Thesis Submitted in Partial Fulfillment of the
Requirements for the Degree of

MASTER OF APPLIED SCIENCE

in the Department of Electrical and Computer Engineering

Spectroscopic Analysis of Samples in Aqueous Environments using a Hollow Core Fiber

by

Akshara Adike
B.Tech, Sri Padmavati Mahila Visvavidyalayam, 2012

Supervisory Committee

Dr. Tao Lu, Supervisor
(Department of Electrical and Computer Engineering)

Dr. T. Aaron Gulliver, Departmental Member
(Department of Electrical and Computer Engineering)

Supervisory Committee

Dr. Tao Lu, Supervisor
(Department of Electrical and Computer Engineering)

Dr. T. Aaron Gulliver, Departmental Member
(Department of Electrical and Computer Engineering)

ABSTRACT

This thesis details the procedure and the results of Raman spectroscopy obtained for graded concentrations of aqueous samples passing through the core of a stand alone hollow core fiber(HCF). Also, spectroscopic analysis of these samples is performed in a HCF coupler fabricated using silica core(SCF) single mode fiber. The SCF-HCF coupler is fabricated using the principle of evanescent wave coupling, enabling the periodic transfer of light between SCF and HCF. With the SCF-HCF coupler, the core of the HCF can be filled with aqueous samples which leads to the change of the light signal propagating through the SCF as a result of the interaction of light with the sample at the coupling region. The study conducted a detailed literature review which led to measuring the back reflections in contrast to the measurement of the forward propagating light upon it's interaction with the sample. After a series of experiments using varying concentrations of samples such as Ytterbium Oxide(Yb_2O_3) suspension, Double Walled Carbon Nanotubes(DWCNT) suspension, aqueous H_2S, aqueous H_2S in DWCNT suspension, it is found that the change in the concentrations of each sample can be identified by measuring the back reflections of the SCF-HCF coupler and the results are repetitive.

Contents

Bibliography 75

List of Figures

ACKNOWLEDGEMENTS

I would like to thank:

Dr. Tao Lu for his valuable guidance, constant support and passion in research to motivate and encourage me as my supervisor through out my degree. His patience and flexibility helped me to work on my studies and thesis in a productive and independent manner;

Alex from CAMTEC, for the help on Raman microscopy facilities;

Sanul Haque, for his continuous and extended help throughout the experiments. .

CONTRIBUTION

T.L. conceived and designed the experiments; A.A. performed the experiments; A.A. and T.L. analyzed the data; A.A. wrote the report.

DEDICATION

Dedicated to my son Lidin, husband and parents for their patience and being my pillars throughout all phases of my research work.

Chapter 1

Introduction

Ever since days of yore, the most vital need of mankind was to communicate with each other, which led to the era to conceptualize and build efficient communication systems to transfer messages or signals from one place to another. Dr. K. C. Kao and his colleagues in 1966 from the Standard Telecommunication Laboratories Ltd. were the first to develop the idea of guiding light within optical fibers [3]. Ever since the onset of optical fiber technology, the optical fibers with glass waveguides carrying light through their length have stepped up the methods of communication systems all over the world. Furthermore over the past three decades, optoelectronics led to the uprise of many inventions due to optimized costs and quality of optoelectronic components [4].

Remote sensing is crucial in applications such as medical, aeronautical, space, oil and gas, construction, etc. There are many hindrances to overcome and be able to survive when sensing in non-ambient conditions. In the field of sensor research and fabrication, enhancements are made to the components used in the sensors. However, these components are also susceptible to the electromagnetic effect from the surrounding environment. These are as well come with higher manufacturing cost considering applications that require thousands of sensors to be multiplexed [5][6] for distributed extended range measurements. Additionally, traditional sensors require higher operating costs and are supposed to be frequently interrogated or decommissioned remotely. Fiber optics for sensing brings out the solutions these problems. Extreme temperature sensing, optimized device costs, multiplexing [5], vast distance interrogation and independence from electromagnetic interference are the characteristic features of fiber optic technology. Moreover, optical fibers are highly compact and very lightweight which enable a very easy integration into any existing structures.

1.1 Advantages of Optical Fiber Sensors

The long established traditional sensor systems have proven to be reliable with reasonable manufacturing costs. Therefore, optical fiber-based sensor systems must display superior advantages over traditional electro-mechanical sensors in order to replace existing conventional sensors. Such advantages that make optical fiber sensors superior include inertness to electromagnetic interference, extreme sensitivity, size [7] and weight, environmental ruggedness [8], multiplexing and distributed capacities [5], etc.

1.1.1 Electromagnetic Interference Inertness

Most fiber sensing heads are basically pure fiber with no electric circuits and hence the external electromagnetic disturbance would not influence the way the light propagates inside optical fibers. Moreover, the sensing information is carried by photons not electrons because the optical fiber sensors are intrinsically not sensitive to electromagnetic interference [8]. This vital feature offers superior advantage of the optical fiber sensors compared to their conventional sensors.

1.1.2 Sensitivity

Since by measuring the change of the light signal, such as the wavelength, phase, intensity, etc., it is easy to achieve high sensitivity with optical fiber sensors. Typically, only a small interference of the working environment would affect the physics of the optical fiber, such as its refractive index, length, configuration, etc., then, these changes in turn, would affect the condition under which the light propagates in fibers. However this can be avoided by properly designing the sensing region.

1.1.3 Lightweight, Small Size, Robustness

Optical fibers have diameters in millimeters, and are extremely lightweight which offers the advantage to be easily embedded [9] into the monitoring systems. Glass in general, is a very stable material [10], which makes these sensors survive under the harsh environment. For instance, in oil well, conditions such as humidity, high temperature and dampness are obstacles for long-time survival of conventional electromechanical sensors where as the optical fiber sensor is passive in nature and hence long-time monitoring can be achieved in the oil wells as required.

1.1.4 Multiplexing and Distributed Capacities

A key application for health monitoring of the huge buildings, such as the dams, bridges, pipelines, requires sensors the ability to continuously monitor with the potential to record and display location of malfunction observed. Optical fibers offers solution to such type of applications. One solution is to deluge sensors to forming a mesh, and then embed into the structures to be monitored to achieve the quasi-distributed sensing [11]. The main advantage of such distributed sensors is that they have simple sensing block which could achieve fully distributed sensing for the case where the positions to be monitored are not known.

1.2 Types of Optical Fiber Sensors

There are many types of fiber optic sensors in market used for wide range of applications [10]. Based on the mode of operation, modulation and demodulation processes, these sensors can be classified as amplitude (intensity), phase modulation(polarization), frequency (wavelength) [10]. All these parameters are due to change upon external perturbations.

$$E(t) = E_p(t) \cos\left[\omega t + \theta(t)\right] \tag{1.1}$$

- Amplitude or intensity varying sensors ($E_p(t)$): They are based on detecting changes in the light intensity, temperature or pressure. These sensors are simple and inexpensive.

- Frequency or wavelength varying sensors ($\omega(t)$): They map the changes in the frequency or wavelength to the measuring parameter. Wavelength measurement is extremely sensitive and is therefore not affected with any fluctuations introduced with input laser light source.

- Phase modulating (Polarization) optic sensors ($\theta(t)$): These type of sensors are generally complicated, hence any changes such as bending, twisting, stretching effects the functionality of the sensor.

Fiber optic sensors used in chemical or biological applications consist of a molecular recognition component and signal transducers. They can be categorized [12] as Direct (intrinsic) and Indirect (extrinsic) sensors as shown below.

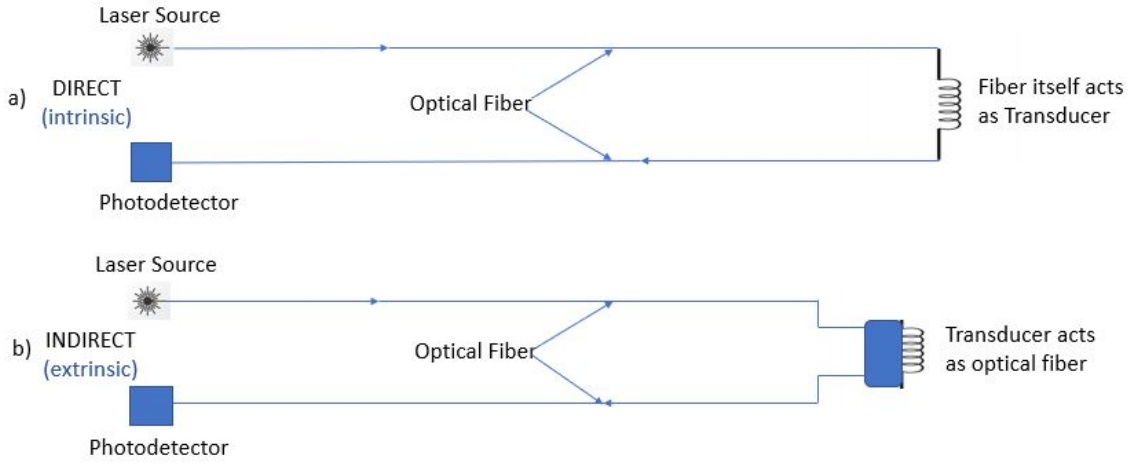

Figure 1.1: a) The light beam does not leave the optical fiber but changes parameters at the sensing region and propagates to the photo-detector. b) Light beam leaves the transmitting fiber at the sensing region and propagates back to the detector fiber

1.3 Optical Fiber Sensors Technologies

1.3.1 Fiber Gratings

Fiber gratings are straight forward, with direct intrinsic [12] sensing components that can be embedded into a silica fiber. This implies a periodic photo structure is inscribed into the core of fiber [13] which will reflect a particular optical wavelength that is dependent on periodicity.

I. Uniform Gratings

Grating is consistent and the modulation of refractive index is uniform [14] along the fiber core axis. Based upon factors such as length of the grating, uniform gratings can be categorised into a) FBG - Fiber Bragg Gratings [8], b) LPG - Long Period Fiber Gratings

a) FBG - Fiber Bragg Gratings

FBG sensor system works on the principal of monitoring the shift in wavelength of output Bragg signal [15].

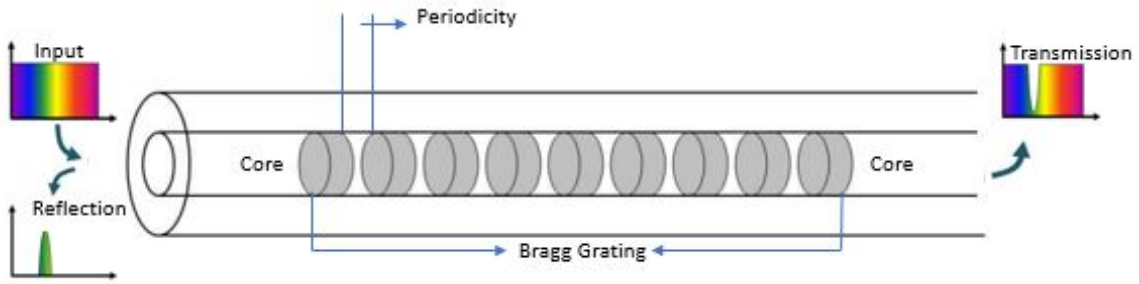

Figure 1.2: Fiber Bragg Grating

The Bragg wavelength (λ_B), or resonance of a grating is

$$\lambda_B = 2n_{eff}\Lambda \tag{1.2}$$

where n_{eff} is the effective refractive index of the core of the optical fiber, Λ is the periodicity of the grating [8]. This simple concept makes it the most popular technique in designing optical sensors. As the input source light propagates through the FBG, a portion of it with a peculiar wavelength known as Bragg Wavelength(BW) is reflected which is caused due to the periodicity(order of 100nm) of the variations in the refractive index(usually between 10^{-5} to 10^{-3}), that remains unaffected as the core is surrounded by cladding [8]. Therefore, methods such as etching [16] are used to expose the evanescent field in the core to the surrounding environment of interest and by studying the wavelength shift, the refractive index of the sample can be analyzed.

b) LPG - Long Period Fiber Gratings

LPGs are similar to Fiber Bragg Gratings(FBGs) except that these have a much longer periodicity ranging between "few hundreds microns" [17]. As this wavelength is comparatively larger than the operating wavelength, they are not reflective type sensors, in contrast to the FBGs. In LPGs the guided mode travelling in the core gets coupled into the cladding at one of the modes at certain wavelengths dependent on factors such as refractive indices, the grating pitch, propagation constants [17]. This coupled light decays exponentially due to the nature of the cladding. This decay is sensitive to the refractive index of the environment surrounding the cladding modes. Hence a change to the refractive index of the environment surrounding the cladding modes causes the deviation of the periodicity of LPG resulting resonance wavelength

shift its position of the output spectrum making them transmission type devices [18]. Since LPGs are made from optical fibers, it offers an advantage of being embedded easily into existing optical devices [19].

II.Non Uniform Gratings

In Non-uniform gratings[1], the grating periodicity and the modulation depth of the refractive index is inconsistent along the core axis of the fiber. There exists many types of non-uniform gratings such as:

Chirped FBGs: The change of refractive index along the fiber core is inconsistent and the grating period decreases in a linear fashion.

Superimposed Multiple FBGs: Several Bragg gratings are embedded at the same location in the core of the optical fiber

Superstructure FBGs: These type of FBGs have the refractive index modulation in a periodically varying manner.

1.3.2 Fiber Optic Coupler

Fiber couplers are extensively used in the field of optics. They find applications in optical sensors, optical amplifiers, fiber gyroscopes, optical LAN and broadcasting networks. They can be used to either split or combine signals. With the splitting functionality, the input signal is split into two or more outputs. In parallel, the optical combiners combine two or more input signals to a single output [20]. These couplers are fabricated by tapering the fibers together, which results in the shrinking of the cladding of the fibers junction where the generated evanescent field gets exposed to the surrounding environment [21]. The transmission spectrum of the fiber optic coupler is sensitive to temperature, bending, strain, pressure etc. Couplers are bi-directional and hence carry light in both directions. Many combinations are possible and two examples are shown in the Fig 1.3.

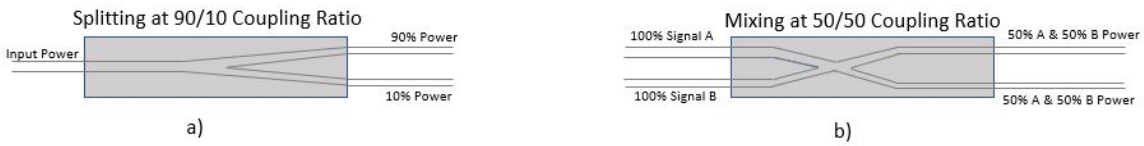

Figure 1.3: a) 1x2 Optical Coupler, b) 2x2 Optical Coupler

The directional couplers can be extended to $i \times j$ where i and j are ≥ 1 and

the number is based on the application. Directional couplers exists in either active or passive form. Active directional couplers use other opto-electronic and optical devices such as photoreceivers, splitters, combiners, etc to propagate and transmit the light whereas passive directional couplers propagate the light directly.

The evanescent field produced in the optical directional couplers would be able to penetrate through the cladding and re-enters the core region. This technique makes these devices to be used as directional coupler sensors [22]. Some other advanced sensors are developed such as mode selective coupler [23], coupling between single mode and photonic crystal fiber [24][25] and broadband coupler [26].

A Fiber optic coupler [27] sensor fabricated via single mode silica core fiber (SCF) and a homemade hollow core fiber (HCF), where the core of the hollow fiber is filled with test samples. Changes in the refractive index or concentrations of samples under test in the core of the hollow fiber modifies the properties of the propagating light within the single mode SCF.

1.4 Hollow Core Fibers (HCF)

In recent times, hollow core fibers (HCF) gained attractions in the optical industry due to the low manufacturing costs and offered solutions to the sensing problems. These are microstructured cladding with hollow core that confines light entirely inside the core. The interaction between the fundamental mode and the cladding (silica) is weak which makes the fiber radiation insensitive. These features are ideal for nonlinear optics, optic gyroscopes, narrow linewidth delivery, gas spectroscopy, sensors etc. using techniques such as Hollow Core Bragg Fiber (HCBFs) [28][29] and Polycrystalline Fibers (HCPCFs) [30]. These fibers are nearly bend insensitive. No change in the optical transmission can be observed even with a bend diameter < 1 cm [30].

The hollow core is designed to allow the flow of test sample (liquid or gas) for sensing. Cladding is made of silica. Fused silica [31] capillary tubing is an example of a type of the hollow core fiber and its structure is shown in the Fig. 1.4. Optical Fiber Couplers are fabricated using tapering of the fiber and the same method is applied to build a SCF-HCF coupler.

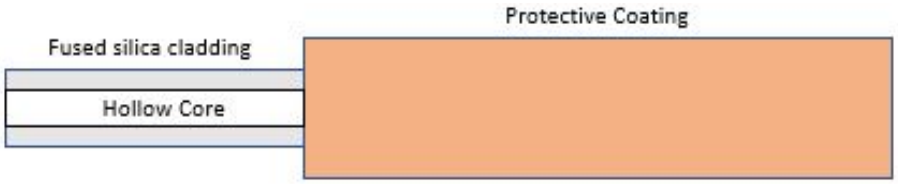

Figure 1.4: Hollow core fiber with fused silica cladding and polyamide protective coating

1.5 Spectroscopy

Spectroscopy is an optical technique used to assess the concentration of a given chemical species in a mixture. It studies the interaction between electromagnetic (EM) radiation and matter of interest. A plot of the response to the radiation as a function of wavelength (λ) or frequency is referred to as a spectrum [32]. Using this technique it is possible to investigate the structures of atoms and molecules in detail, including the electron configurations of atoms such as ground and excited states, physical properties, chemical chains and reactions within the molecule [32]. Spectroscopy is used in every research field of science which involves quantitative analysis of matter and hence has wide range of applications ranging from astronomy to identify the chemical makeup, properties, temperature and sometimes the velocity of the celestial objects, improve the structure of drugs in pharmaceutical industry, pathogen identification in biomedical industry, toxic or heavy metals identification in food beverage industry.

Figure 1.5: Spectrometer reads the signal from the sensor and displays the signals on GUI to analyse the sample

Fig 1.5 shows a light source as the input signal to the optical fiber, which can be laser or white light depending on the application and the sample of interest. This guiding light in the optical fiber changes its properties at the sensing region where the sample is introduced. This change in the input signal is captured by the spectrometer and the signal is interrogated for further analysis of the sample. The primary detection methods of optical spectrometry include photoconductive (semiconductor), photoemmissive (photomultipliers), photographic (films). An edge of using this tech-

nique is that the entire spectrum can be obtained in parallel, and if low-intensity spectra exists,it can readily be taken using sensitive film.

Essentially, two things can happens when the sample of interest is hit by light. The sample either emits or absorbs light. In case of absorption, the sample absorbs a part of energy of the incident light. During emission, the sample emits a wavelength in contrast to the incident light. Fluroscence, phosphorescene, luminescence can be explained with emission spectra. The effect of light on sample depends on factors such as wavelength/intensity of light, what it does to the molecules/atoms of the sample. Spectroscopic methods can be broadly classified into the following types:

- Spectroscopy Based on Absorption/Emission [33]: The emission and absorption spectra of elements depends on the structure of atom/molecule. In case of atoms, the atoms move to the excited state by absorbing photons from the incident light and the excited atom relaxes spontaneously to the ground state with the emission of photons. Each transition correlating to the emission or absorption of energy will represent a spectral line on the spectra. On the other hand, the mechanism of molecular spectra is similar to the atomic spectra with added complexities. These complexities arise due interactions of the various nuclei of atoms of same element or different elements in contrast to the atomic spectra.

- UV/Vis Spectroscopy [34]: An element concentration in a mixture can be determined based on the absorption of UV or Visible radiation. This spectroscopy technique is popular and common because most of the organic and inorganic elements have strong and sensitive absorption bands at the UV/Vis region in the electromagnetic spectrum. If the sample does not absorb or absorbance is weak in the UV/Vis region, it is always feasible to add another element that helps in identifying the sample of interest.

- Photo-luminescence Spectroscopy [35]: Photoluminescence spectroscopy can be classified into Fluorescence and Phosphorescence. In an atom, a pair of electrons in the same ground state have opposite spins and exits in a Singlet Spin State. When the sample absorbs UV/Vis photon, one valence electron changes from ground to the excited state while conserving the electron spin. In such case, emission of photon when the electron transits between two energy levels with the same spin state is called *Fluorescence* and the probability of achieving it is

high. However it decays rapidly once the excitation source is removed because the average lifetime of an electron in the excited state is only 10^{-5} to 10^{-8}s. Counter to it, when the emission occurs between two energy levels that differ in their respective spin states is *Phosphorescence*.

- Raman Spectroscopy [36]: When the incident light hits the sample molecules(solid, liquid or gaseous phase), majority of photons are either scattered or dispersed at the same energy as the incident photons which is termed as elastic scattering or Rayleigh scattering. However, a small percentage of these scattered photons, approximately 1 in 10 million photons scatter at a different frequency than the incident photon called as Raman effect. Raman provides edge to the users to collect information about the presence and vibrational signature of interrogated molecule, giving insight into the molecule structure and interactions with the other molecules around it. Hence, Raman spectroscopy is a positive identification of an element and the size of the peaks in the spectrum represents the amount of it in the sample or mixture.

- Fourier Transform Infrared spectroscopy (FTIR) [37]: In FTIR infrared light passes through a Michelson interferometer along the optical path. The Michelson interferometer consists of a moving mirror, fixed mirror and a beam splitter. The beam splitter in the interferometer is used to split the light into two which is then reflected from the moving and the fixed mirror before being recombined again. Due to the reciprocating movements made by the moving mirror, there occurs a change in the optical path difference to the fixed mirror, such that there exists a phase difference changes with time. The output intensity from the interferometer is recorded in an interferogram. This signal is Fourier transformed and represented as Wavenumber (/cm) vs Transmission.

- X-Ray Diffraction [38]: This type of spectroscopy is a popular and common technique to study the crystalline structure and the unit cell dimensions. This is based on the constructive interference of the X-rays that are monochromatic with the the crystalline sample.

1.5.1 Electromagnetic Spectrum

The EM spectrum is the composition of Electric (E) and Magnetic (H) waves oscillating perpendicular to each other and travel in a defined direction. In EM radiation,

one can quantify the amount of energy of radiation if the light wave is considered as a stream of particles called *photons* instead of a wave. Energy of a wavelength is

$$E = \frac{hc}{\lambda} \tag{1.3}$$

E: Energy(kJ/mol), λ: Wavelength, c: speed of light (3x10^8 m/s), h: 6.62607004 10^{34} Js Plancks constant.

Each category of wavelengths is the EM spectrum are different due to differences in the corresponding energies as shown in Fig.1.6. From the energy equation, it is evident that the shorter the wavelength higher the energy.

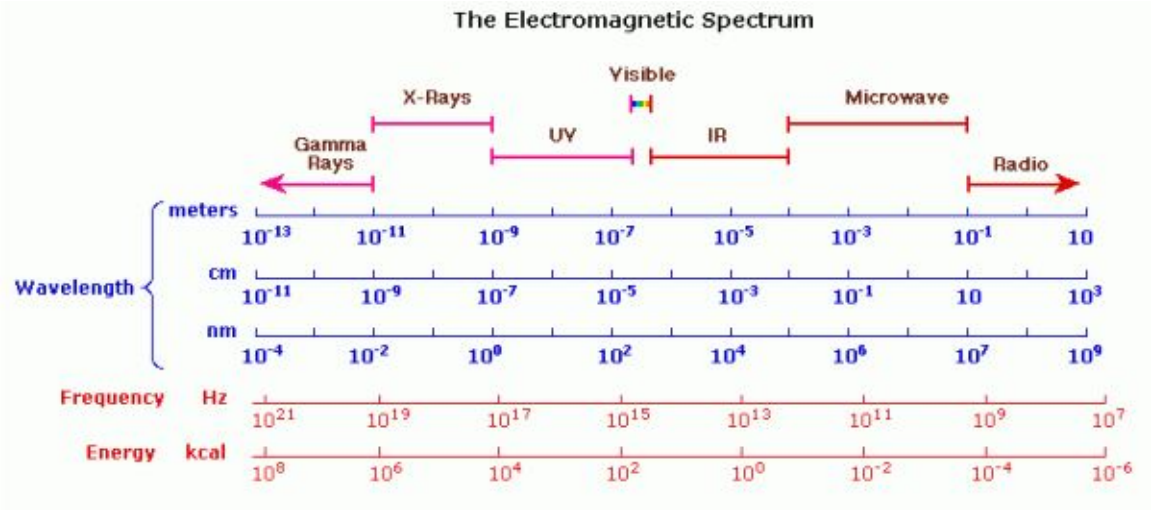

Figure 1.6: Full range of wavelengths of the EM spectrum [1]

The following table lists the commonly used spectroscopic techniques, the category of EM radiation involved and the type of energy transfer upon the radiation of light.

Type of Energy Transfer	Region of EM Spectrum	Spectroscopic Technique
Absorption	γ-ray	Mossbauer spectroscopy
	X-ray	X-ray absorption spectroscopy
	UV/Vis	UV/Vis spectroscopy
	IR	Raman and IR spectroscopy
	Microwave	Microwave spectroscopy
	Radio wave	Electron spin spectroscopy
emission (thermal excitation)	UV/Vis	Atomic Emission Spectroscopy
Photoluminescence	X-ray	X-ray fluorescence
	UV/Vis	Phosphorescence spectroscopy
Chemiluminescence	UV/Vis	Chemiluminescence spectroscopy

1.6 Research Objective

It can be concluded that fiber optic sensors provide advantages over conventional electro-mechanical sensors. Considering the edges of optical sensors, a fiber optic sensor is proposed which uses the similar concept of directional coupler i.e. evanescent wave coupling. The proposed optical fiber coupler sensor [39] is fabricated using a hollow core fiber and a silica core fiber following the procedure outlined in Chapter 2. The percentage of light evanescently coupled from single mode fiber to hollow core fiber and back to single mode fiber depends on the concentration of the sample inside the core of the HCF at the coupling region. In particular, the main objective of this thesis study was:

To perform Raman spectroscopy for varying concentrations of samples of interest flowing through case(i): core of a free standing HCF, case(ii): core of HCF in a SCF-HCF coupler and identify the change in intensity w.r.t the concentration of the sample passed in both the cases

The basis to develop this objective is that existing conventional methods/sensors have many requirements particularly in the areas where (1) a large amount of samples is required, (2) impact of the surrounding test environment (3) size, reusablity, complexity of the hardware and software to analyse the sample.

Contribution

The following four samples were proposed to perform the experiments in both cases. The samples are aqueous H_2S, Yb_2O_3 suspension, Double Walled Carbon Nanotubes(DWCNT)

suspension and DWCNT suspension in aqueous H_2S. These samples are diluted further from their original concentrations as detailed in the later sections of the thesis. Raman spectrocopy is done for each sample concentration and the results are explained in the results chapter of the thesis.

1.7 Thesis Outline

This thesis focuses on the fabrication of a SCF-HCF coupler sensor which identifies the change in concentration as a function of intensity of the input light.

Chapter 1 provides the general theory of sensors and the advantages of fiber optic sensors over conventional sensors. This chapter gives insight to the role and importance of types of spectroscopy in analysing the sample of interest using the fiber optic sensors.

Chapter 2 explains the principle of operation of evanescent wave sensors, obtaining an expression to describe evanescent wave, understanding the concept of coupling behind fabrication of SMF-HCF coupler, packaging the coupler.

Chapter 3 lists and explains the procedures of the experiments performed, concept of circulator and its role in the measurements, mathematical calculations and preparation guidelines of graded concentrations of each sample used in the thesis.

Chapter 4 elaborates Raman spectrocsopy, principle, applications. Raman spectroscopy is performed on every prepared concentration of given sample and the results obtained are compared with published data .

Chapter 5 explains the principles of absorption spectroscopy, understanding of the Beer-Lambert law, concept of back reflection, importance and it's measurement using optical circulator, coupler experiments.

Chapter 6 provides conclusions and scope for research work is discussed.

Chapter 2

Background Theory

Optical sensors based on intensity modulation directly depend on the optical properties of the measurand. The light intensity is changed within the optical fiber when the sensing region encounters the sample of interest [40][41]. The change of this light intensity is recorded and displayed using a spectrometer. By studying the change in the input intensity, the concentration of the sample used can be analysed. These sensors offers the advantage of its simplicity of signal processing, robustness and ease of fabrication. One example of such type of sensors is the Frustrated Total Internal Reflection (FTIR) [40]. This works on the principle of evanescent wave coupling created by the concept of total internal reflection. The following sections give detailed explanation of the concepts of Total Internal Reflection (TIR) and Evanescent wave coupling.

2.1 Principle of Optical Fiber Guidance

2.1.1 Light Propagation Inside Optical Fiber

Standard optical fibers propagate the input light using the principle of total internal reflection. A regular optical fiber has a core and a cladding with the core on a slightly higher refractive index than the cladding, and the ratio of the two indices determines the angle at which light within the core becomes totally internally reflected at the core/cladding boundary thereby blocking the transmission of light into the cladding. This angle is known as the critical angle θ_c.

$$\sin(\theta_c) = \frac{n_{cladding}}{n_{core}}$$

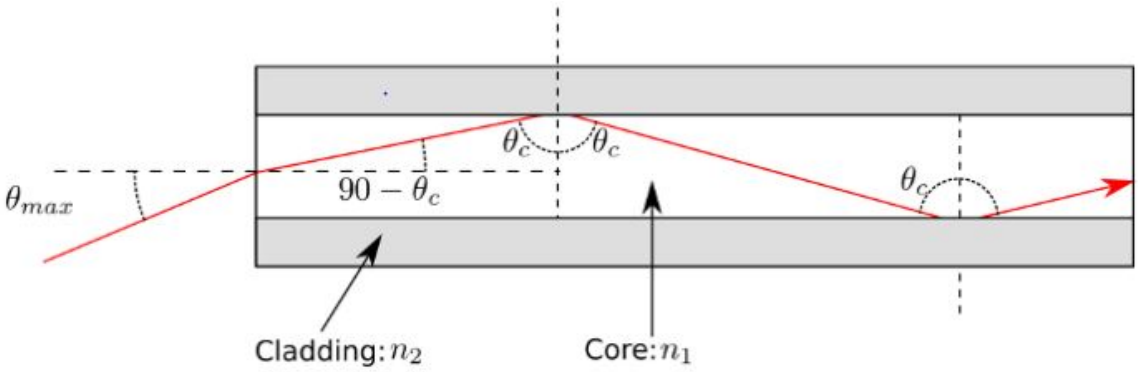

Figure 2.1: "Transmission of light on a slab waveguide using the concept of Total Internal Reflection"

The total internally reflected light will then propagate down the core of the fiber as represented in the Fig 2.1 [1]. The pattern and the shape of the light intensity profile is referred to as a mode. The modes of an optical fiber are finite and are determined by factors such as the core and cladding refractive indices, size of core, the shape of the refractive index profile, and the wavelength or frequency of light. The solutions for a wave equation in optical fiber take the form of Bessel functions which can be used to calculate the number of modes a given fiber can support. The normalized frequency, or V-number, can be used to determine the number of modes that a fiber can guide. For a step-index fiber

$$V = \frac{2\pi}{\lambda} a \sqrt{{n_{cladding}}^2 - {n_{core}}^2} \tag{2.1}$$

where V is the normalized frequency, λ is the wavelength of light, $'a'$ is the radius of the core. With V $\leq$ 2.405, the fundamental mode can only be guided, and the fiber is referred as single mode. For V $\geq$ 2.405, multiple modes can be guided and propagate along the optical fiber. For multimode fibers that support many modes, the V-number is approximately equal to the number of guided modes. Therefore, optical fibers can be exclusively designed to support a specified number of modes at a given wavelength by varying the core size and the refractive index of the core and cladding. The optical fibers discussed throughout this thesis are single mode silica core (SCF) optical fibers.

2.1.2 Evanescent Wave Propagation

Ideally, entire incident light should propagate inside the core of the fiber, however the electromagnetic theory of light refers to the concept of leakage of some part of light to the cladding at the interface region during the total internal reflection and decays exponentially as represented in the Fig 2.2. This field is known as an evanescent field or wave.

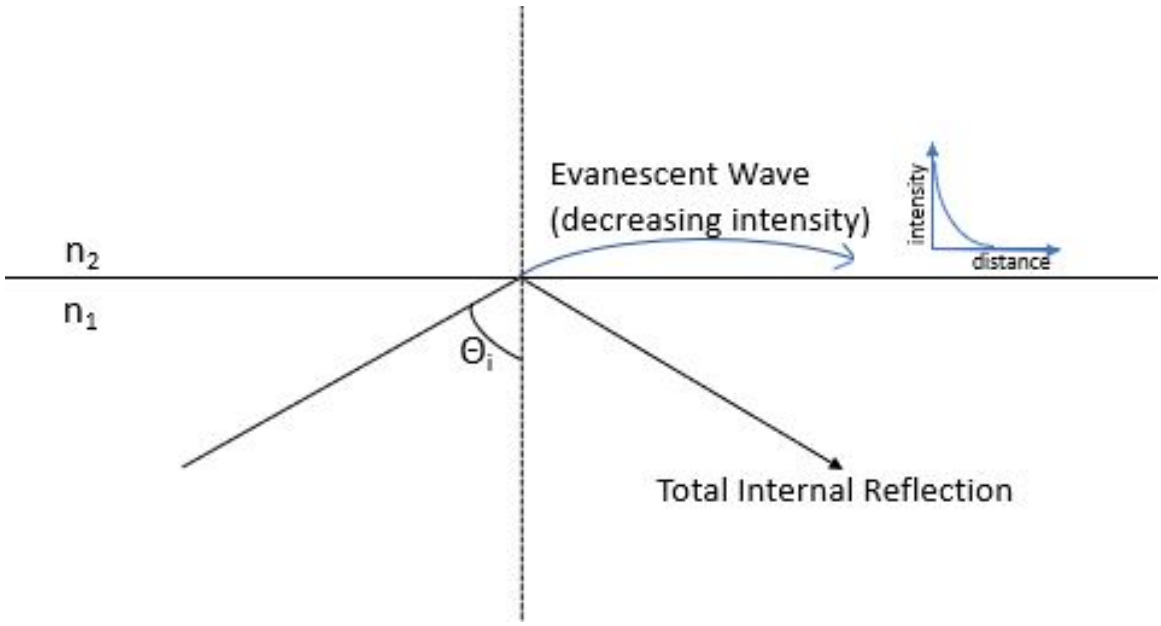

Figure 2.2: The arrow in the medium(n_2) represents the exponentially decaying evanescent wave with the distance travelled.

The penetration depth [42] of the decaying evanescent field is given by

$$d = \frac{\lambda}{4\pi\sqrt{{n_1}^2 \sin^2(\theta_i) - {n_2}^2}} \tag{2.2}$$

where λ is the wavelength of the light, n_1 and n_2 are the refractive indices of medium 1 and 2 and θ_i is the incident angle as represented to Fig 2.2.

The evanescent field (I) decays exponentially along the propagating direction (z) from the core-cladding interface region according to $I_z = I_0 \times e^{-z/d}$, where I_0 is the intensity at the core-cladding interface region.

2.2 Directional Coupler

Total internal reflection and the evanescent coupling between two fibers are the building concepts of a directional coupler. As detailed in the previous section, upon the satisfaction of the critical angle condition, propagation of light happens through the core of the fiber due to total internal reflection. These propagating light rays are referred to as **Modes**. The propagation of only one light ray is possible given the core diameter is small according to 2.1. Since only single mode propagates through the core diameter, such fibers are termed as Single Mode Fibers. During mode propagation in the core of the fiber, there exists a leakage of light that expands into the cladding region called **evanescent wave.** The mathematical representation of the propagation of the light is done using the Maxwell's equations through Modal Analysis.

2.2.1 Modal Analysis - Maxwell's Equations

Time harmonic [43] Maxwells equations for linear, isotropic, non-conducting and non-magnetic medium in terms of phasor form are

$$\nabla \times \vec{E} = -j\omega\vec{B} \tag{2.3}$$

$$\nabla \times \vec{H} = j\omega\vec{D} \tag{2.4}$$

$$\nabla.\vec{D} = 0 \tag{2.5}$$

$$\nabla.\vec{B} = 0 \tag{2.6}$$

where $\vec{D} = \epsilon\vec{E}$, $\vec{B} = \mu\vec{H}$, $\epsilon = \epsilon_o\epsilon_r$ (ϵ_o: permeability of vaccum, ϵ_r: permeability of material) , $\mu = \mu_o\mu_r$ (μ_o: permittivity of vaccum, $\mu_r = 1$: relative permittivity of the material as it is non-magnetic domain).
Using the equations derived in [44] to describe the modes in optical fibers, modal analysis of the above mentioned time harmonic [43] Maxwell's equations from 2.3 to 2.6 is performed
Applying curl operator to equation 2.3 and expanding the left hand side gives:

$$\nabla \times (\nabla \times \vec{E}) = \nabla(\nabla.\vec{E}) - \nabla^2\vec{E} \tag{2.7}$$

Inserting $\vec{D} = \epsilon\vec{E}$ in eq. 2.4 we obtain:

$$\nabla.\vec{E} = -\frac{\nabla\epsilon_r}{\epsilon_r}.\vec{E} = 0 \tag{2.8}$$

Substituting equation 2.7 in equation 2.6 we get:

$$\nabla(\frac{\nabla\epsilon_r}{\epsilon_r}\vec{E}) + \nabla^2\vec{E} + k_o^2\epsilon_r\vec{E} = 0 \tag{2.9}$$

where k_o(wavenumber of the vaccum) is given by

$$k_o = \omega\sqrt{\epsilon_o\mu_o} = \frac{\omega}{c} \tag{2.10}$$

and the wavenumber k in of the propagating medium is:

$$k = k_o n \tag{2.11}$$

Considering ϵ_r is piecewise homogeneous, then the equation 2.8 can be reduced further to obtain Helmholtz equation for electric field as follows:

$$\nabla^2\vec{E} + k^2\vec{E} = 0 \tag{2.12}$$

Similarly, Helmholtz equation for magnetic field can be derived into:

$$\nabla^2\vec{H} + k^2\vec{H} = 0 \tag{2.13}$$

$\vec{E}$ and $\vec{H}$ in above derived Helmholtz equations are the functions of 3-dimensional space coordinates and k is a wave number.

The electric filed phasor of the single mode fiber and the hollow core fiber used in the thesis can be given by:

$$\vec{E} = \vec{E}(x, y)e^{-j\beta z} \tag{2.14}$$

where z is the direction of wave propagation independent of the variations in the refractive index in the x and y directions. Using, variable separation method, separating z from x , y coordinates , and substituting $\frac{\partial}{\partial z} to - j\beta$ and the three dimensional Laplace operator ∇^2 in the Helmholtz equations 2.11 and 2.12. The Laplace operator ∇^2 is further split into $\nabla_\perp$ and ∇z where $\nabla_\perp$ represents the transverse part of the

cross sectional coordinates x , y and ∇z is the longitudinal coordinate.

$$\nabla^2 \vec{E} = (\nabla_\perp^2 - \beta^2)\vec{E} \tag{2.15}$$

The waveguides of the optical fiber are cylindrical coordinates, hence as $\nabla_\perp^2$ in equation 2.15 is replaced by $\nabla_\perp^2 = \frac{1}{r}\frac{\partial}{\partial r}(r\frac{\partial}{\partial r}) + \frac{1}{r^2}\frac{\partial^2}{\phi^2}$ Substituting equation 2.14 in 2.11,

$$\nabla_\perp^2 \vec{E}(x,y) + (k^2 - \beta^2)\vec{E}(x,y) = 0 \tag{2.16}$$

Similarly, for magnetic field we obtain the following equation:

$$\nabla_\perp^2 \vec{H}(x,y) + (k^2 - \beta^2)\vec{H}(x,y) = 0 \tag{2.17}$$

Equations 2.15 and 2.16 represents six second order differential equations for E(x, y) and H(x, y) with three components each that are related to each other. In order to obtain the solutions to each of the component, initially two components, for example: the longitudinal components E_z and H_z are considered as independent. Once these components are solved, using Maxwell equations, the solutions to the each component E_x, E_y, H_x, H_y can be derived as following:

$$E_x = -\frac{1}{k^2 - \beta^2}(j\beta\frac{\partial E_z}{\partial x} + j\omega\mu\frac{\partial H_z}{\partial y}) \tag{2.18}$$

$$E_y = -\frac{1}{k^2 - \beta^2}(j\beta\frac{\partial H_z}{\partial y} - j\omega\mu\frac{\partial H_z}{\partial x}) \tag{2.19}$$

$$H_x = -\frac{1}{k^2 - \beta^2}(j\beta\frac{\partial E_z}{\partial x} - j\omega\epsilon\frac{\partial E_z}{r\partial y}) \tag{2.20}$$

$$H_y = -\frac{1}{k^2 - \beta^2}(j\beta\frac{\partial H_z}{\partial y} + j\omega\epsilon\frac{\partial E_z}{\partial x}) \tag{2.21}$$

With the help of the above equations we can use equations 2.15 and 2.16 to analyse the wave behaviour as following:

- $E_z = 0$, $H_z \neq 0$: Transverse Electric (TE) modes (transverse modal field)
- $E_z \neq 0$, $H_z = 0$: There will be a magnetic field component missing in the modal field distribution. These are called Transverse Magnetic (TM) modes.
- $E_z \neq 0$, $H_z \neq 0$: These types of modal field distributions are called Hybrid Modes.

2.2.2 Principle of Operation

From the previous section, we understand that an evanescence field exists outside any dielectric waveguide which is cladding in case of the optical fiber. When the cores of two fibers are placed close to each other, parts of the propagating electromagnetic field overlap spatially that results in the periodic transfer of power between these two cores due to mode coupling in the two cores. Usually the gap required [43] between the two cores is dependent on the mode size, penetration depth. When two non-identical single mode fibers with propagation constants β_1 and β_1 are coupled, then at any given point z on the fiber, the power propagating[44] in these two fibers is given by:

$$\frac{P_1(z)}{P_1(0)} = 1 - \frac{\kappa^2}{\gamma^2}\sin^2\gamma z \tag{2.22}$$

$$\frac{P_2(z)}{P_1(0)} = \frac{\kappa^2}{\gamma^2}\sin^2\gamma z \tag{2.23}$$

where $P_1(0)$ is the power launched into one of the fiber, fiber 1 at $z = 0$, $\gamma^2 = \kappa^2 + \frac{1}{4}(\Delta\beta)^2$, $\Delta\beta = \beta_1 - \beta_2$ and κ is the coupling coefficient which determines the efficiency of coupling between two fibers, β is referred as *phase mismatch*. According to the conservation of power, $P_1(z) + P_2(z) = P_1(0)$ independent of z. The power exchange between the two fibers is said to be completed when their propagation constants are equal. On contrary, there exists a periodic yet incomplete exchange of power between the two fibers when their propagation constants are unequal.

2.2.3 Case(i): Phase match condition ($\Delta\beta = 0$)

$$P_1(z) = P_1(0)\cos^2\kappa z \tag{2.24}$$

$$P_2(z) = P_1(0)\sin^2\kappa z \tag{2.25}$$

Periodic exchange of power happens between two fibers when

$$z = 0, \frac{\pi}{\kappa}, \frac{2\pi}{\kappa}, ... = \frac{m\pi}{\kappa}; m = 0, 1, 2, .. \tag{2.26}$$

$P_1(z) = P_1(0)$ and $P_2(z) = 0$: entire power in one of the fibers

$P_1(z) = 0$ and $P_2(z) = P_1(0)$: entire power is in another fiber

The minimum distance between the fibers to be maintained such that the power

transfer from one fiber to another takes place completely is given by:

$$L_c = \frac{\pi}{2\kappa} \tag{2.27}$$

Hence large κ means small coupling length L_c.

2.2.4 Case(ii): Non-Phase match condition ($\beta_1 \neq \beta_2$)

The hollow fiber coupler sensor used in this thesis relies on this condition because the propagation constants of the silica core fiber (SCF) and the hollow core fiber (HCF) are different. The fabrication of this sensor is explained in the next section of this chapter. At $\beta_1 \neq \beta_2$, the maximum power transferred from the the SCF to HCF is given by:

$$\eta_{max} = \frac{P_{max}^{HCF}}{P_{in}^{SCF}} = (\frac{\kappa^2}{\gamma^2}\sin^2\gamma z)_{max} = \frac{1}{1+(\Delta\beta/2\kappa)} = \frac{\kappa^2}{\gamma^2} \tag{2.28}$$

where, P_{max}^{HCF} is maximum power in hollow core fiber
P_{in}^{SCF} is the input power in the silica core fiber

After interacting with the test samples in the hollow core fiber (HCF), the light power will be transferred back to the silica core fiber (SCF) at its maximum $z = \frac{\pi}{2\gamma}$ and assuming the coupling length to be L_c, the power exiting the SCF would be $\frac{\kappa^2}{\gamma^2}\sin^2\gamma z$ in the case of coupling between SCF-HCF [45].

2.3 Fabrication: Hollow Core Fiber Sensor

2.3.1 Preparing the Hollow Core Fiber

Specifications of the hollow core fiber

The hollow core fiber (HCF) for the fabrication of the sensor used in this thesis is the silica capillary tubing from Polymicro Technologies whose cladding is made of fused silica. The specifications of the HCF are as follows [46]:
Inner diameter i.e diameter of the hollow core is 320μm
Diameter including the hollow core, cladding and the polyamide coating is 430μm
The thickness of the polyamide coating is 16.8μm

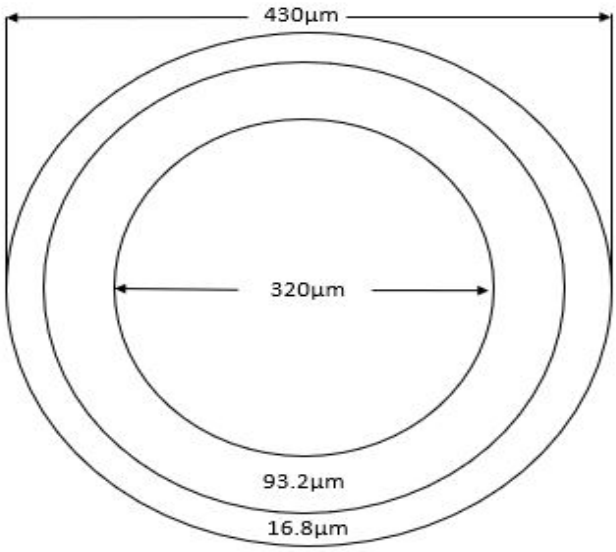

Figure 2.3: Dimensions of the hollow core fiber.

Polyamide coating removal

The hollow core fiber comes with a polyamide coating to protect it from external abrasions and it's removal is dependent on the sensor's application. Several techniques are currently in use to remove[31] the coating. Thermal techniques include using flame sources such as lighters, hydrogen or propane flames, immersing the hollow core fiber for 2 to 5 minutes in sulfuric acid at 150^{o}C or etching using Hydrogen Fluoride(HF). Laser can also be used to remove the polyamide coating, however it requires extreme precision and control during the process.

2.3.2 Preparing Single Mode Silica Core Fiber

Silica core single mode fiber-SM800 (SCF) from Thorlabs® is used as the primary fiber which propagates the input light with the refractive index of the inner core being 1.48 and the outer cladding being 1.44. For evanescence to happen, the cladding of the silica core fiber must be exposed so that there exists a leakage of the propagating wave. The acrylic coating is stripped off the cladding using fiber stripper. One end of the fiber is connected to the laser source and the other end is connected to Newport optical power meter 1830c to record the changes in the input power during the fabrication process. However, it can also be connected to a photo-detector and then to the oscilloscope which could display the changes in the input signal (in terms

of voltage) during the coupling procedure.

2.3.3 Fusing HCF with the Single Mode SCF

Hollow core coupler sensor is a 2×2 optical directional coupler and is fabricated via hydrogen flame based process. Extreme care was taken to avoid scratches or defects on the fusing region of the hollow core fiber and the single mode fiber during the process of removing the protective coating over them. The stripped region of the SCF where the cladding region is exposed, is twined with caution on the stripped region of the HCF which is shown in the Fig. 2.4. Since the radius of bending in the hollow core fiber is much greater than the single mode fiber, the SCF is wound over the HCF. This is then carefully placed into the V-grooves of the fiber holding magnetic

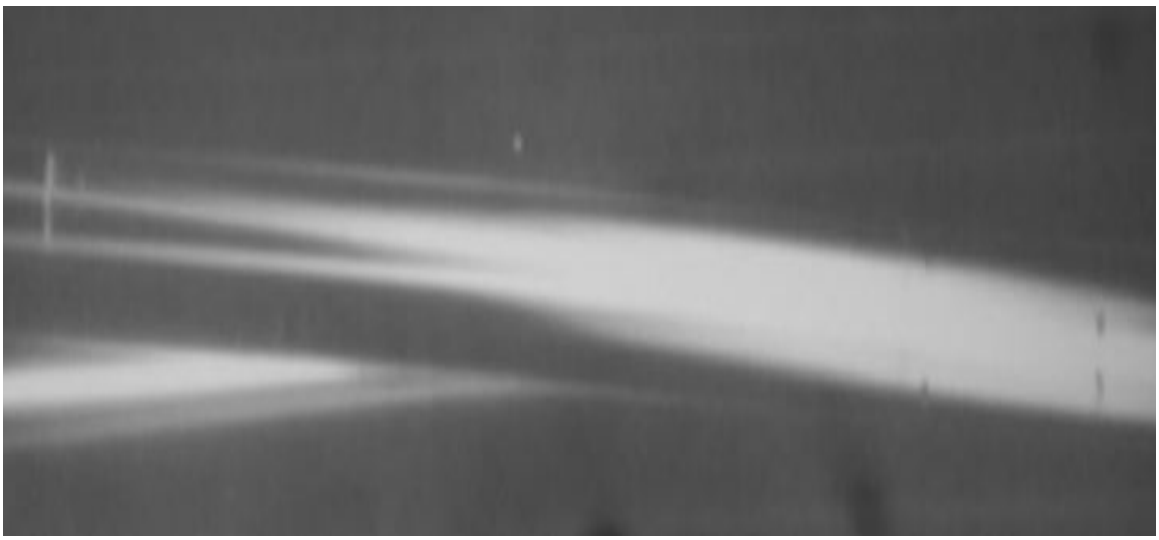

Figure 2.4: Image on the microscope showing the twisted pair of SCF-HCF, held tightly in the V-grooves of the fiber pulling stage

clamps(Thorlabs®) that hold the fibers tightly during fusing. Hydrogen flame from underneath, points to the fibers at the twisted region. The fibers are pulled apart on regulated speed with a consistent hydrogen flame. The coupler pulling station is shown in Fig. 2.5.

Each side of the magnetic clamps is driven by stepper motor controlled by the graphical LabView program. This program records the pulling distance of the clamps from the stepper motor and the change in the power of the light propagating in the primary SCH from the optical power meter. Initially, the hydrogen flame is turned on to heat and melt the twisted region of the fibers. The motors are then

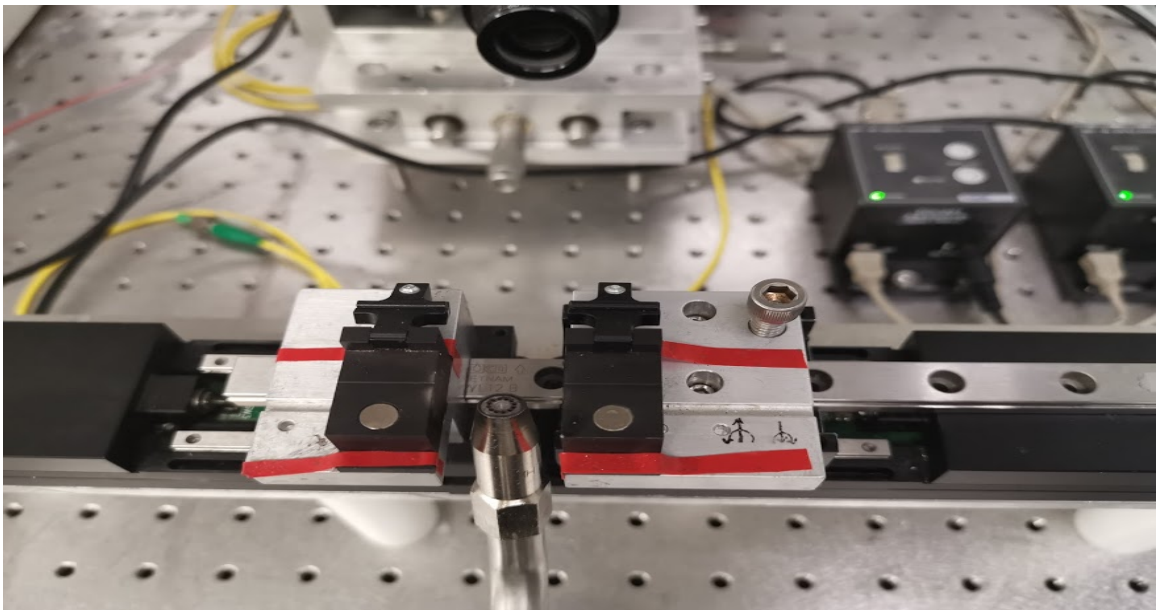

Figure 2.5: Fiber pulling station showing the magnetic clamps on either side that hold the fibers with a constant hydrogen flame source from underneath.

switched on using Thorlabs® APT software (LabView) pulling both the left and right magnetic clamps evenly in their respective directions. As a result, coupling through evanescence takes place as explained in section 2.2. The output of the optical power meter is recorded using data acquisition device (DAQ USB-6211) and controlled by the custom built labview program.

2.3.4 Packaging the Fabricated Coupler

The fused region after coupling is about 1 to 2 μm in diameter and is sensitive to external perturbations such as dust particles settling on the fused region can mislead the data obtained for the sample. Hence, the fused region should be enclosed. It should be made sure that the enclosed medium is neutral to electromagnetic radiation. For this purpose, a special type of PDMS (polydimethylsiloxane) from ML Solar is used. Epoxy was initially considered for packing purposes. However, noise is observed in the data recorded and also it is not optically transparent. It is identified that the Epoxy used also interacted with the light signal and hence false results of the test sample.

PDMS (Polydimethylsiloxane)

PDMS belongs to a group of silicones and has applications ranging from medicals to cosmetics. In optics, it has a major use in fabrication of microfluidic devices due to its desirable properties such as transparency and inertness to chemical and electromagentic radiations [47]. These features offer the solution to fabricate the HCF-SCF coupler as PDMS can withstand high temperatures and exhibits minimal aging. The PDMS used for fabricating the HCF coupler is from ML Solar labs that is used to stick the solar panels and hence is an absolute insulator for electromagnetic radiation.

The fabricated coupler is carefully placed onto a sterile microscopic glass slide leaving a gap between the glass slide and the fabricated region of the fiber. The part A and part B of the PDMS is taken in 10:1 ratio respectively and mixed thoroughly. The PDMS mixture is carefully dropped onto the glass slide covering the entire fabricated region of the coupler in it as shown in the fig 2.6 The PDMS has to be dripped layer

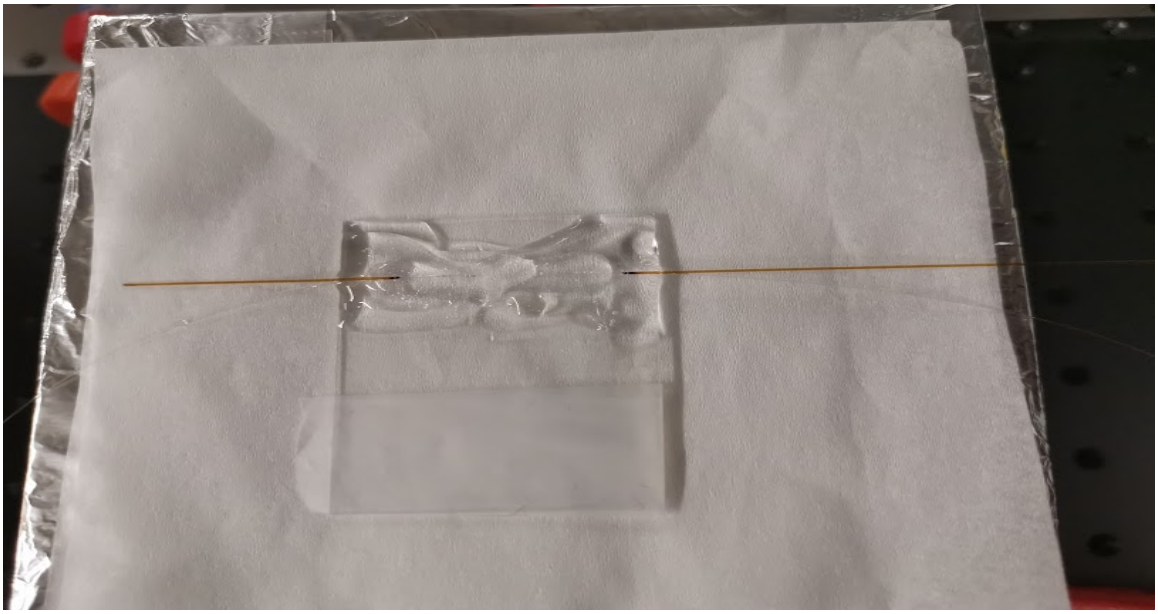

Figure 2.6: Cured PDMS enclosing the sensing region of the coupler

by layer onto the Microscopic glass slide else flooding the sensing region with PDMS at once would result in pressure on the coupling region. This could lead to breaking of the fiber. Furthermore, it takes around 24 hours under ambient conditions for the PDMS to harden. Using a microheater(MINCO ASI15901R19.7XSB 1009) solves the problem. The microheater is placed under the glass slide and a constant temperature

of 100^{o}C is applied. This dramatically brought down the wait time from 24 hours to 1 hour. The packaged coupler was used for several experiments for different samples and the results are analysed in the following chapters.

Chapter 3

Procedures of Sample Preparations

As discussed in the research objective, graded concentrations of Yb_2O_3 suspension, aqueous Hydrogen Sulfide (H_2S) water, Double-walled carbon nanotubes suspension, aqueous H_2S in 10nM suspension of DWCNT are proposed as samples. Each of these four different sample are further diluted as per the calculations detailed in the following sections to inject through the core of HCF to obtain the spectral data of each sample. The concentration calculation and preparation of each sample is explained below.

3.0.1 Yb_2O_3 suspension preparation

Yb_2O_3 suspension used in this thesis is from Sigma Aldrich labs: product no: 641928-25mL. From the specification sheet [48] of the product, the concentration of Yb_2O_3 is 5 wt% distribution in H_2O, which implies the suspension is composed of 95% water and 5% of Yb_2O_3. The concentration of the original Yb_2O_3 suspension is calculated as

$$Density(Yb_2O_3) = \frac{Mass_T}{V_T} \tag{3.1}$$

where Mass_T = 100g which is the total mass of the suspension considering 5wt% dispersion of Yb_2O_3 in water,
V_T is the total volume of suspension
V_T = Volume of Yb_2O_3+ Volume of H_2O
Volume of Yb_2O_3 = Mass of Yb_2O_3/Mass Density of Yb_2O_3 = 0.545 mL
Given, Mass of Yb_2O_3 = 5g and Mass Density of Yb_2O_3 = 9.17 g/mL.

$V_T = 95.545\,\text{mL}$
where Volume of $H_2O = 95\,\text{mL}$
Hence

$$Density(Yb_2O_3) = 1.04\,g/mL \tag{3.2}$$

Given the diameter of the Yb_2O_3 nanoparticle from the specifications of product is 80nm. Volume V_{np} of single nanoparticle is given by

$$V_{np} = \frac{4 \times \pi \times r^3}{3} = (2.682 \pm 0.002) \times 10^5\,nm^3 \tag{3.3}$$

We find the mass of single nanoparticle of Yb_2O_3 using

$$M_{np} = Density(Yb_2O_3) \times V_{np} = (2.459 \pm 0.003) \times 10^{-15}\,g \tag{3.4}$$

Calculate the number of particles in the mass(5g) of Yb_2O_3 as

$$N_{particles} = \frac{Mass(Yb_2O_3)}{M_{np}} \simeq 2.03 \times 10^{15} \tag{3.5}$$

The total number of particles/mL of suspension is given by

$$\frac{N_{particles}}{mL} = \frac{N_{particles}}{V_T} \simeq 2.12 \times 10^{13} \tag{3.6}$$

Finally, the concentration(C) of Yb_2O_3 suspension is obtained using from the above derived parameters as

$$C = \frac{N_{particles}/L}{Avogadro\,No} = 35\ \pm\ 0.004\,nM \tag{3.7}$$

where Avogadro No = 6.023x10^{23} particles/mol. Using eq.3.8, the concentration dilution table for Yb_2O_3 suspension table is.

$$C_1V_1 = C_2V_2 \tag{3.8}$$

C_1: Initial concentration
V_1: Initial volume
C_2: Final concentration obtained by diluting C_1
V_2: Volume of the final concentration

Initial Concentration	Volume of Yb_2O_3	Volume of H_2O	Final Concentration
35 nM	285.7 μL	714.3 μL	10 nM
10 nM	100 μL	900 μL	1 nM
1 nM	100 μL	900 μL	100 pM
100 pM	100 μL	900 μL	10 pM
10 pM	100 μL	900 μL	1 pM
1 pM	100 μL	900 μL	100 fM

3.0.2 Hydrogen Sulfide(H_2S) Water Preparation

Hydrogen Sulfide samples used in the coupler experiments are from LabChem product LC154702. It is a mixture [49] of 99.6% of water and 0.4% of H_2S gas. Using the following procedure, it was found that the molar concentration of the original mixture is 117.3mM. This hydrogen sulfide water is further diluted into the concentration of 100mM, 10mM, 1mM, 100μM, 10μM, 1μM, 100nM, 10nM, 1nM, 100pM using the serial dilution method to prepare 1mL of each of the above given concentrations.

Total volume of solution = 500 mL.

$$Volume\% = \frac{V_{solute}}{V_{solution}} \times 100 \tag{3.9}$$

Volume of solute (V_{solute}) is given by

$$V_{solute} = \frac{0.4 \times 500}{100} = 2mL \tag{3.10}$$

Volume of solution ($V_{solutiom}$) is given by

$$V_{solution} = \frac{99.6 \times 500}{100} = 498mL \tag{3.11}$$

Calculating moles of solute(H_2S) by

$$M_{solute} = \frac{Mass_{solute}}{MolarMass_{solute}} = \frac{2g}{34.1g/mol} = 0.0586 \pm 0.0003mol \tag{3.12}$$

Therefore the Molarity (M) of the mixture is,

$$Molarity(M) = \frac{M_{solute}}{V_{solution}(L)} = \frac{0.0586\,mol}{0.5L} = 117.302 \pm 0.001\,mM \simeq 117.3\,mM \tag{3.13}$$

Using 3.8, it is calculated that 852.5μL of 117.3mM H_2S should be mixed with 147.5μL of Deionised Distilled H_2O to obtain 1mL of 100mM H_2S water. Similary, equation 3.8 is used to prepare the remaining concentrations of H_2S via series dilution method. For concentrations below 100mM, the volume of deionised distilled Water used for dilution is kept constant at 900μL and is mixed with the calculated H_2S to dilute to a lower concentration. The concentrations and the volumes of H_2S and H_2O used are tabulated as follows:

Initial Concentration	Volume of H_2S	Volume of H_2O	Final Concentration
117.3mM	852.5μL	147.4μL	100mM
100mM	100μL	900μL	10mM
10mM	100μL	900μL	1mM
1mM	100μL	900μL	100μM
100μM	100μL	900μL	10μM
10μM	100μL	900μL	1μM
1μM	100μL	900μL	100nM
100nM	100μL	900μL	10nM
10nM	100μL	900μL	1nM
1nM	100μL	900μL	100pM

3.0.3 Double-Walled Carbon Nanotubes Suspension Preparation

Double walled carbon nanotubes from Sigma Aldrich product:755141-1G, are used in the coupler experiments. Using the following approach, 2.26mg of DWCNT was used to prepare 100nM suspension of CNT in water. Again, series dilution method is followed to further decrease the concentration the descending order and is tabulated as follows. From the specs [50] of Sigma Aldrich, the radius of concentric double walled CNT is 1.75nm, length of the DWCNT is 3μm. Therefore, the Volume(V_{DWCNT}) and Mass(M_{DWCNT}) of each DWCNT is

$$V_{DWCNT} = \pi r^2 h = 2.887 \times 10^4\,nm^3 \tag{3.14}$$

and

$$M_{DWCNT} = Density_{DWCNT} \times V_{DWCNT} = 3.75 \times 10^{-25}\, g \tag{3.15}$$

Number of particles in a suspension is

$$\frac{Mass(DWCNT)\, suspension}{M_{DWCNT}} = \frac{Mass}{3.75 \times 10^{-25}} \tag{3.16}$$

We can calculate the concentration(C) of a mixture given the number of particles/L by

$$C = \frac{No.\, of\, particles/L}{Avogadro\, No} = \frac{Mass/L}{6.023 \times 10^{23}} \tag{3.17}$$

The required concentration is 100nM, then the calculated Mass of DWCNT required to prepare 1mL of suspension is 0.0022596 ± 0.000004 grams i.e. 2.26mg. The dilution table for DWCNT from 100nM to 100pM is given below

Initial Concentration	Volume H_2O	Volume DWCNT suspension	Final Concentration
100nM	900μL	100μL	10nM
10nM	900μL	100μL	1nM
1nM	900μL	100μL	100pM
100pM	900μL	100μL	10pM
10pM	900μL	100μL	1pM

3.0.4 Aqueous H_2S in 10nM DWCNT Suspension Preparation

100nM concentration of DWCNT suspension is prepared following the steps as explained in the previous section. This suspension is then used to prepare graded concentrations of H_2S in 10nM DWCNT suspension and the calculations are as follows:

Step 1: Prepare graded concentrations of H_2S solution as explained in section 3.0.2. All the concentrations(100mM, 10mM, 1mM, 100μM, 10μM, 1μM are prepared to a volume of 1mL each.

Step 2: Remove 100μL from each of them, making them 900μL of each concentration

Step 3: Prepare 10nM concentration of 1mL DWCNT suspension as detailed in the section 3.2.3.

Step 4: Add 100μL of 10nM DWCNT suspension(from step 3) to the H_2S samples

from step 2.

Step 5: We get 117.3mM, 100mM, 10mM, 1mM, 100μL, 10μL, 1μL concentrations of H_2S in 10nM suspension of DWCNT each being 1mL.

Concentration(H_2S)	Volume(H_2S)	Volume(DWCNT)	Concentration(H_2S+DWCNT)
117.3mM	900μL	100μL	100mM
100mM	900μL	100μL	10mM
1mM	900μL	100μL	100μM
100μM	900μL	100μL	10μM
10μM	900μL	100μL	1μM

All the samples were prepared carefully in a sterile environment. A series of experiments was performed to record and analyse the data obtained for each sample concentration. It should be noted that for the coupler experiments the needle-syringe set is replaced with for every concentration with the sample to avoid all possible contamination. The following experiments were done to measure the data for the above prepared samples.

1. Raman spectroscopy is performed on the concentrations of Yb_2O_3 within the core of HCF and for the samples placed on the microscopic glass slide at the operating wavelengths of 532nm.

2. Raman peaks are identified for DWCNT and and are analysed at the operating wavelength of 532nm.

3. Identify H_2S from H_2O on different concentrations H_2S water using Raman spectroscopy at the wavelength of 532nm.

4. Perform Raman on aqueous H_2S in DWCNT suspension and analyse differences from the results obtained from the Raman of plain H_2S water.

5. Measure the spectrum by recording the back reflections of the each concentration of Yb_2O_3 suspension, DWCNT suspension, aqueous H_2S, aqueous H_2S in DWCNT suspension with a tunable 815nm-855nm laser source operated at 829.60nm.

The procedure followed and the results obtained for each concentration of all the samples used in both Raman and coupler experiments are analysed in the later chapters.

Chapter 4

Raman Spectroscopy

4.1 Introduction

Spectroscopy is the fingerprint [32] of a material, disclosing the elements in the material and its quantity. Spectroscopy offers the advantage to detect the presence of an element by not getting in direct contact with it. Almost anything that either absorbs, emits or reflect light can be used for spectroscopic analysis [51]. As mentioned in section 1.5, not just the identification of elements but also information about the makeup of the elements such as electrons, atomic nuclei and molecules can be obtained.

The relation between wavelength and frequency is

$$\nu = \frac{c}{\lambda} \tag{4.1}$$

where ν: frequency in cycles/second, c: velocity of light in vaccum, λ: wavelength. It should be noted that, practically there does not exists the actual divisions between the frequencies in the electromagnetic spectrum, however the radiations gradually blend into one another [51].

4.2 Interpretation of Spectral Information

It is known since the beginning of spectroscopy that the spectrum of an element is same regardless of the quantity of it. This means each atom of that element would exhibit all of the emission or absorption lines in the spectrum. When molecules are involved, a band spectrum is produced rather than the line spectrum but the principle is same for both. However, under high dispersion the band spectra exhibits

line spectra [51]. The only effect of increasing or decreasing the sample of interest is increasing or decreasing of the intensity of the lines in the spectrum [51][52][53]. Hence the implication is very clear that if a tiny amount (scale of number of atoms) of each element exhibits the complete spectrum, then a mechanism exists in each atom/molecule to make this possible. According to Neils Bohr, with a proper amount of energy an electron can jump from its current orbit to a higher orbit. However, the excited electron in its unnatural orbit quickly falls back to its original orbit with the emission of energy that was gained during excitation. This energy is a packet of electromagnetic energy called a *photon*. Using equation 1.3 and 4.1, the energy of a photon is given by,

$$E = h\nu \tag{4.2}$$

where E: energy of the photon, h: Planck's constant, ν: frequency.

The participating atoms emit or absorb energy which is equal to the difference between the two excitation energy levels. If E_1 and E_2 represent the upper and the lower energy states, then the amount of energy lost or gained is given by

$$E = h\nu = E_2 - E_1 = h(\nu_2 - \nu_1) \tag{4.3}$$

Hence the transition of electrons between different energy levels give rise to either emission or absorption of radiation with a frequency related to the energy change given in by the equation 4.3.

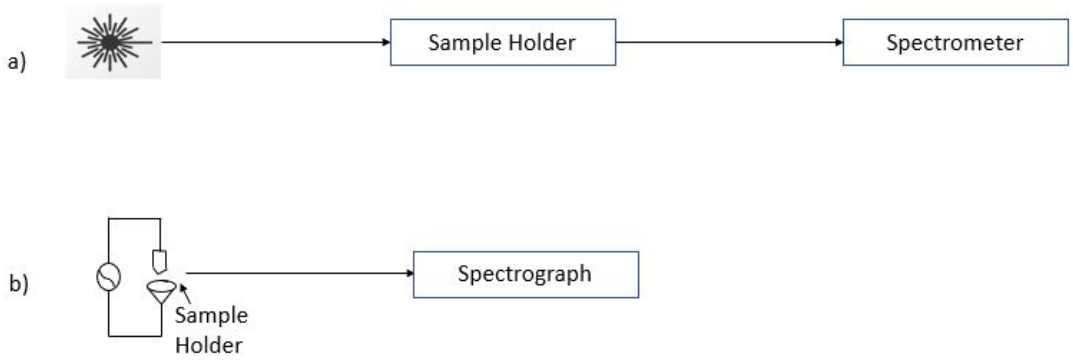

Figure 4.1: a) Absorption Spectroscopy (continuous spectrum), b) Emission Spectroscopy Line Spectrum

4.3 Raman Spectroscopy

Raman spectroscopy is contrary to the rule that the transitions occurs only with the right amount of the input energy to produce or absorb the photons [51]. Under specific conditions, the incident frequencies can be partially absorbed causing the molecules to rotate or vibrate. These photons are scattered with a frequency other than that of the input frequency, represented by Raman line, that is lower in frequency than the original photons and equal to the difference between the incident and the vibrational or rotational frequency [51][52][53]. This is graphically represented in Fig. 4.2. Stokes

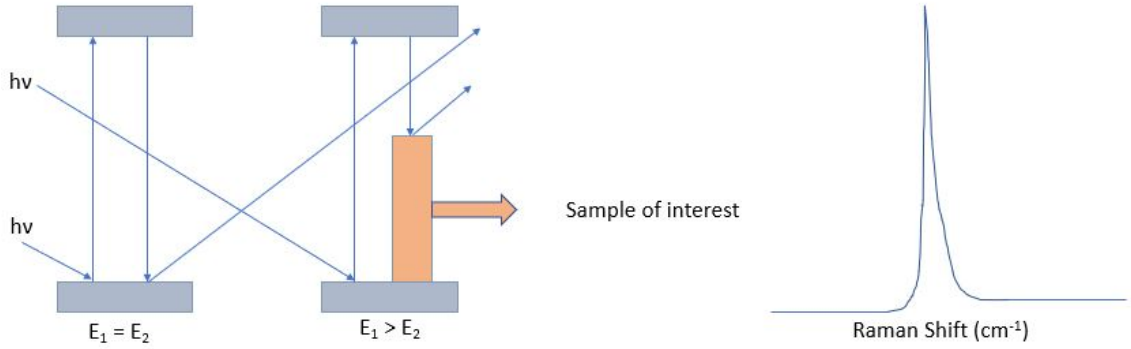

Figure 4.2: Raman spectroscopy principle

scattering [53] happens when the change of energy in the scattered photon is less than the incident one. Some molecules in the sample of interest can initially begin in a vibrationally excited state and later advanced to a higher energy state that can be virtual. These tend to relax into a final energy state which is lower than the initial excited energy state. This type of scattering is called anti-Stokes [53].

Raman mainly considers the changes in molecular bonds which are causes due to the changes in the electron cloud distribution in a molecule as a result of the interaction of light with it. Molecular bonds have certain energy transitions and when a change occurs, Raman modes occur. Examples of molecular bonds with Raman spectral bands are molecules that contain bonds between same nuclear atoms such as Carbon-Carbon. As Raman is a weak effect, the equipment of a Raman Microscope should be well matched to the samples of interest and optimized accordingly. Fig. 4.3 (energy diagram) explains the Rayleigh and Raman scattering

Raman spectroscopy was performed for all concentrations of each sample prepared in the laboratory. Raman spectroscope used in this thesis is inVia^{TM} Qontor® Con-

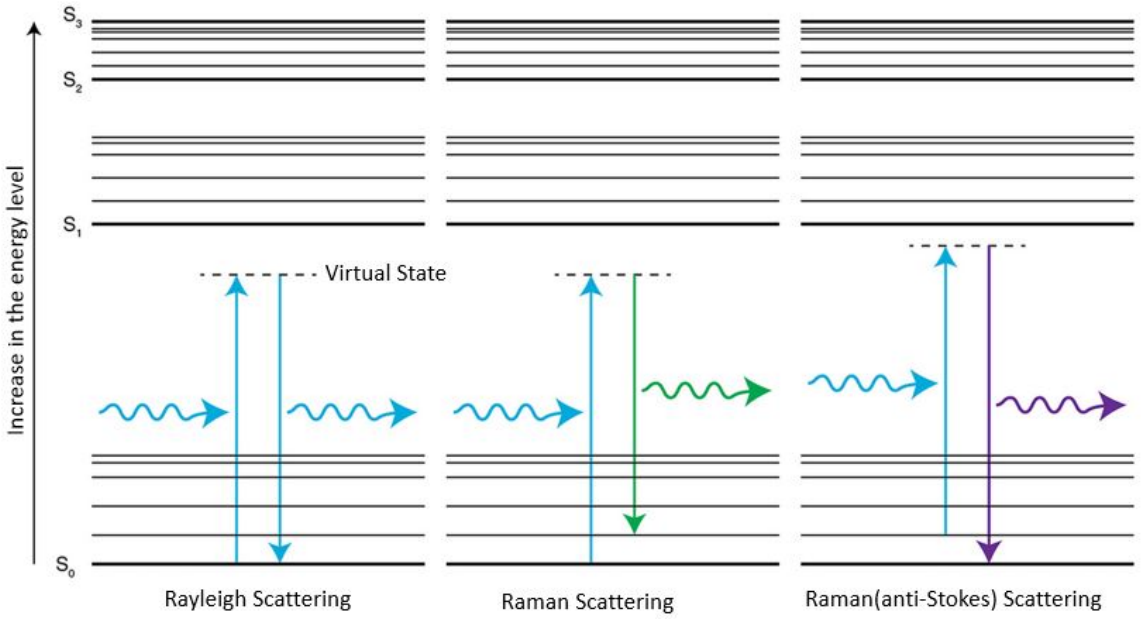

Figure 4.3: Energy levels of Raman, Rayleigh and anti-Stokes scattering.

focal Raman microscope with the courtesy of CAMTEC at Department of Chemistry, University of Victoria. Optimum focus was maintained in the real time along the data collection and white light is used for viewing purposed. This helps avoids the time required to manually focus the laser beam on the sample. The operating wavelengths of Raman microscope are 532nm, 633nm and 785nm. It should be noted that the resolution of the data for each operating wavelength is different though the Numerical Aperture (NA) of the microscope is consistent throughout the experiment. This is because the resolution [54] is wavelength dependent and given by,

$$Resolution(r) = \frac{\lambda}{2NA} \tag{4.4}$$

The laser was focused on the samples with a 0.55 NA and 50x LWD. The laser spot diameter [55] at the probed area of the sample is,

$$D_{laser(spot)} = \frac{1.22\lambda}{NA} \tag{4.5}$$

Hence, the Resolution (r) of the data and diameter of spot size the data obtained with the numerical aperture (NA) of the microscope being 0.55 at the wavelengths 532nm, 633nm, 785nm are given in the table.

Laser Wavelength(nm)	Resolution(nm)	Diameter(spot size) nm
532nm	483.63	1180
633nm	575.45	1404.1
785nm	713.63	1741.2

4.3.1 Raman Spectroscopy: Experiment Setup

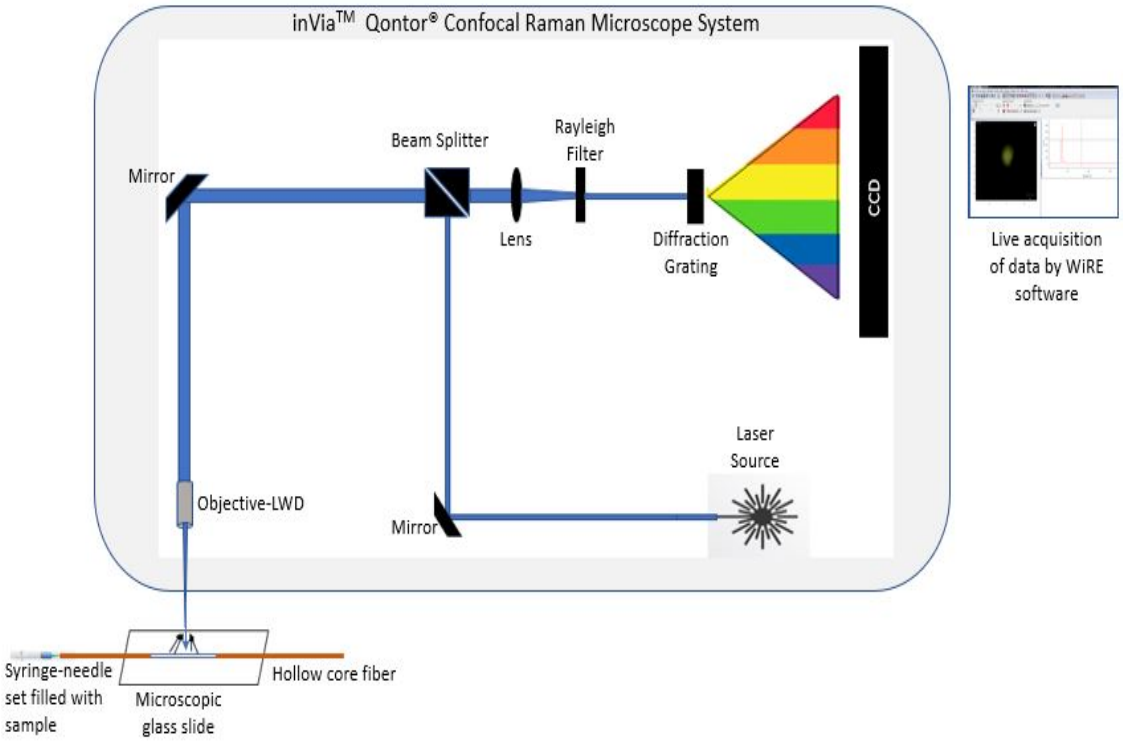

Figure 4.4: The Raman measurement setup.

4.3.2 Calibration of Raman Microscope

The Renishaw Confocal Raman microscope was first calibrated using a silica wafer. The silica wafer was initially focused using white light as shown in Fig. 4.5.a. Then the laser shutter was opened to let the laser beam strike the surface of the silica wafer. The Normalized Raman spectrum of the silica wafer obtained using the Renishaw Confocal Raman microcope using 532nm, 633nm, 785nm is shown in Fig. 4.5.b. The peak at 520.7 is identified as published in [56][55]. This is the prominent peak of Silica. The intensity of the peak is above 12000 (counts of intensity). The x-axis of

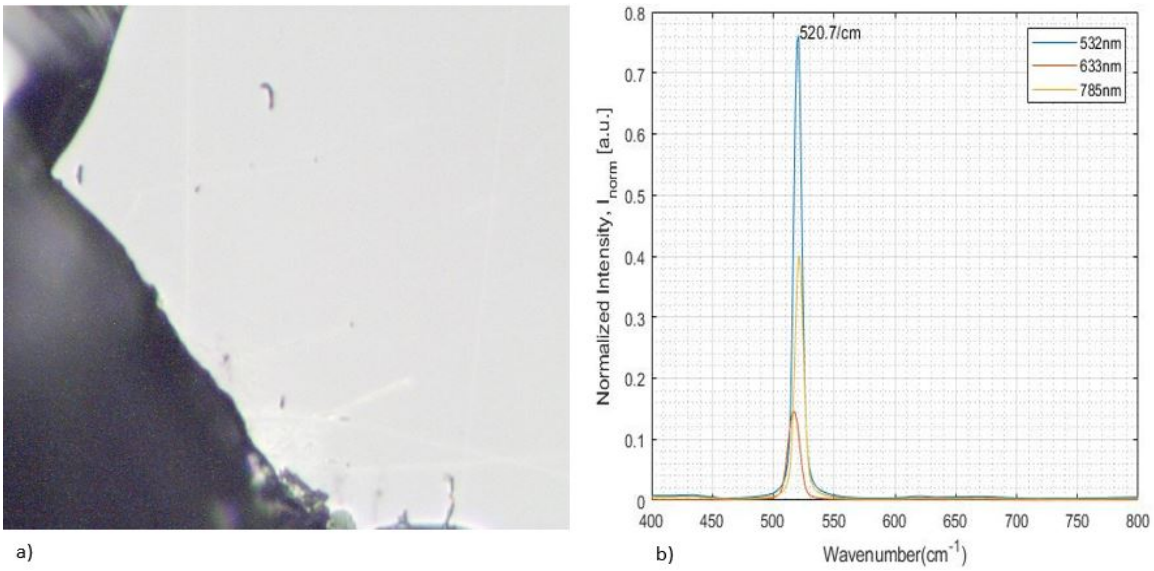

Figure 4.5: a) Image of silica wafer focused with white light, b) Normalized Raman Spectrum for Silica wafer at operating wavelengths of 532nm, 633nm, 785nm.

the normalized Raman spectrum is represented as the wavenumber shift of Raman for convenience. However, wavenumber (Raman shift cm^{-1}) can be converted to wavelength (cm) using the following equation

$$\lambda_{Raman} = \frac{1}{\frac{1}{\lambda_{ex}} - \frac{RamanShift(cm^{-1})}{10^7}} \tag{4.6}$$

where λ_{Raman} is the calculated Raman wavelength; λ_{ex} is the operating wavelength; Raman shift(cm^{-1}) is the wavenumber obtained

The lasers are switched on about 1 hour prior to the experiment. Each concentration of Yb_2O_3, DWCNT, H_2S, H_2S in DWCNT suspension measurements is scanned thrice with each scan lasting about 120 seconds and an exposure time of 10 seconds. Long working distance [57] (LWD) lens from Nikon is used for all the measurements in the thesis. This is because the samples used in the thesis are in aqueous form and needed long working focal distance to be focused inside the liquid sample.

4.3.3 Intensity Normalization of the Raman Spectrum

Depending on the purpose of Raman data analysis, different methods such as multiplicative scatter correction, standard normal variance scaling and polynomial fitting etc are used. However, the purpose of normalization in this thesis is to identify the

percent increase in Raman intensity in relation to the increase in concentration of the sample of interest. Hence a basic normalization procedure is followed which involves normalizing the intensity (y-axis) and the wavenumber (x-axis). The maximum value of the Raman peak of each concentration is taken, followed by identifying the maximum intensity among these maximum values. This maximum value for each same sample, is taken as a dividend for the spectrum of each concentration and the curve is further smoothed using the *smooth* function in Matlab during data processing. All the processing of the data in this thesis is done using *Matlab*.

4.4 Raman Spectroscopy of Ytterbium Oxide(Yb_2O_3)

4.4.1 Ytterbium Oxide(Yb_2O_3): Background

Ytterbium Oxide(Yb_2O_3) is a rare earth oxide. It exists in powder form and the outer layer tarnishes rapidly when exposed to air [58]. Hence it is generally stored in deionised distilled water. As it is highly insoluble thermally stable it forms a suspension rather then a solution. Ultra pure Yb_2O_3 has many applications in optics such as optical amplifiers in lasers [59]. Yb_2O_3 exists in both crystalline and amorphous form. Raman spectrum of crystalline Yb_2O_3 is different from amorphous due to the lattice structures are different in both the forms [59]. From the Raman spectrum obtained in experiment, it is identified that Yb_2O_3 is amorphous [60]. Here, Raman data is recorded on the graded concentrations of Yb_2O_3 suspension as well as dried Yb_2O_3 [59]. Differences in the spectrum are identified and analysed in later parts of this section.

4.4.2 Procedure: Raman for Yb_2O_3 suspension in HCF

Step 1: Small region of HCF is stripped and is placed on a sterile microscopic glass slide using a tape to fix it on the glass slide as shown in the Fig. 4.6.
Step 2: Laser of 532nm is selected and focused on the core of the HCF with its focus point is being viewed in the WiRE (Windows-based Raman Environment) software that is used to control the Raman Spectroscopy system as shown on the right side of Fig. 4.6.
Step 3: Deionized Distilled(DD) water is used as a blank group. DD water is injected into the core of the HCF and is passed through the entire length of the fiber. Laser

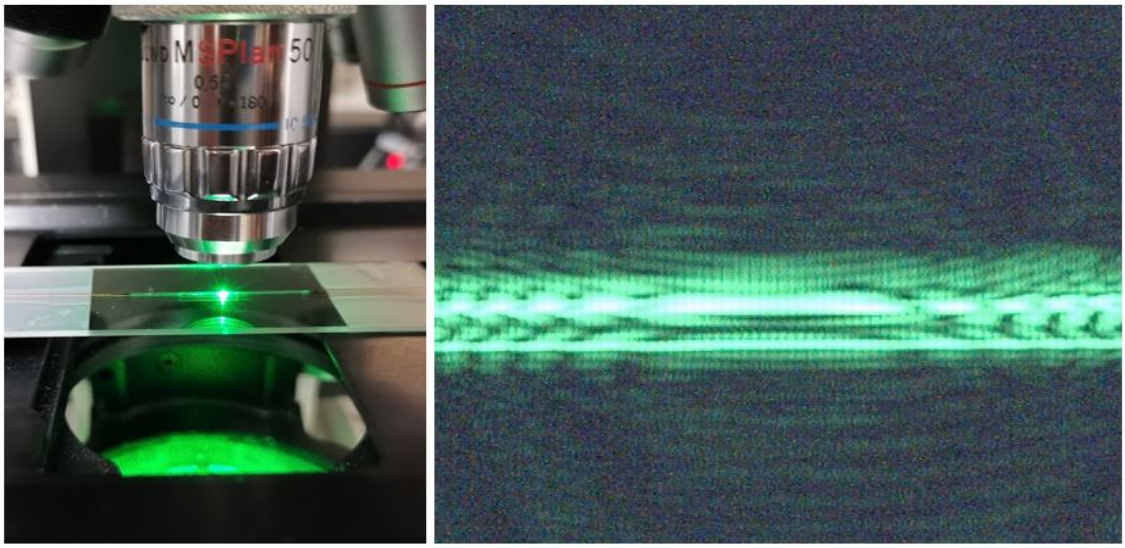

Figure 4.6: Focused laser(532nm) beam in the core of the HCF

was focused on the core column which is filled with DD water.
Step 4: Three scans were recorded with a laser exposure time of 10s and each scan lasting about 3 minutes.

Scanning Modes of Raman System

There are two scanning modes for the Renishaw Raman system used for the current research. **Extended scanning mode** is used to scan the test sample over a wide range of spectrum, mostly between 100 cm $^{-1}$ to 4000 $^{-1}$. This is generally used when the test sample is present in aqueous environments to identify the Raman peaks of water in w.r.t the test sample. **Static scanning mode** is used to check or identify the presence of an element is the sample environment if the exact region of the Raman peak is known. This is done by selecting the center of the static mode with the published peak and scanning around that centre region. **Step 5:**Extended scan mode is used in the range of 100 cm $^{-1}$ to 4000 $^{-1}$. 10% of the original power of laser is selected for recording the data with is 6mW with the original power of the laser beam is 60mW.
Step 6: Similar to the previous step, 1pM, 10pM, 100pM, 1nM, 10nM, 35nM samples of Yb_2O_3 suspension are injected into the core of HCF in the respective order and the data is recorded as explained in the step 4.

4.4.3 Procedure: Raman Spectroscopy of Yb_2O_3 in Powder Form on Microscopic Glass Slide

Step 1: 1mL suspension of original concentration(35nM) Yb_2O_3 is centrifuged for 20minutes. Heavy Yb_2O_3 settles to the bottom of the sample tube.
Step 2: DD water in the suspension is carefully removed. The settled Yb_2O_3 is directly placed onto the surface of a sterile microscopic glass slide.
Step 3: The microscopic glass slide with Yb_2O_3 on its surface is then placed onto a hot plate and is heated at 120^{o}C for 10 minutes. This evaporates all the water molecules and a thin residue remains on the slide.
Step 4: Data is recorded at the operating wavelength of 532nm with the parameters of the Raman system fixed as used for recordings in section 4.4.2 with the exception that the scan mode is changed to static centered at 700cm $^{-1}$

A comparison of the Raman spectra obtained for Yb_2O_3 suspension and powdered form of Yb_2O_3 is explained in the next section.

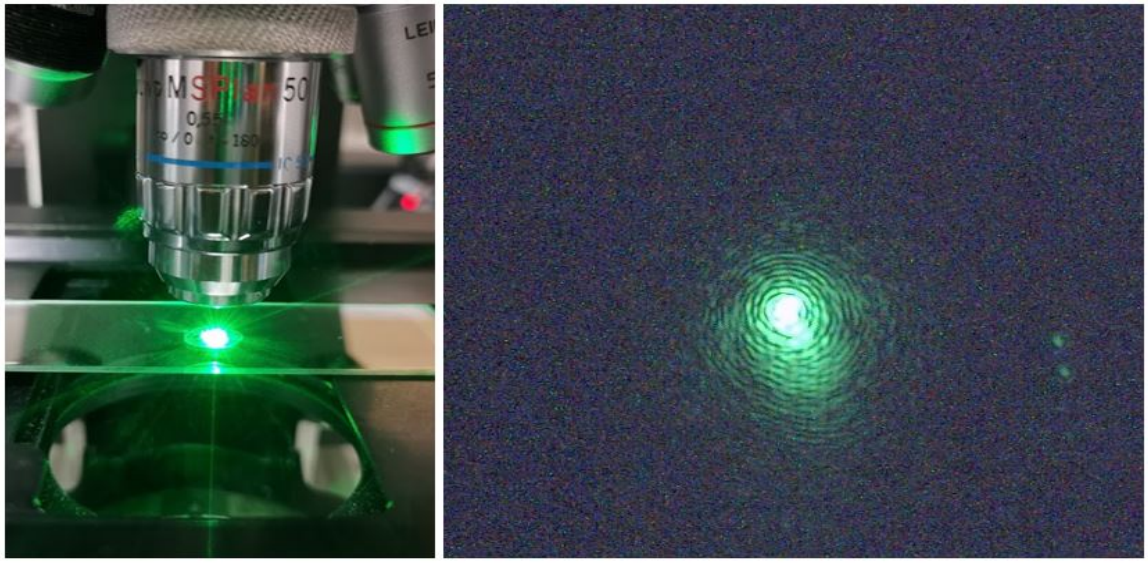

Figure 4.7: Focused laser(532nm) beam on Yb_2O_3 film.

4.4.4 Results

The Raman plot in Fig. 4.8 shows data of the Yb_2O_3 suspension for various concentrations at 532nm in the core of the Hollow Fiber. The plots shows a characteristic peak

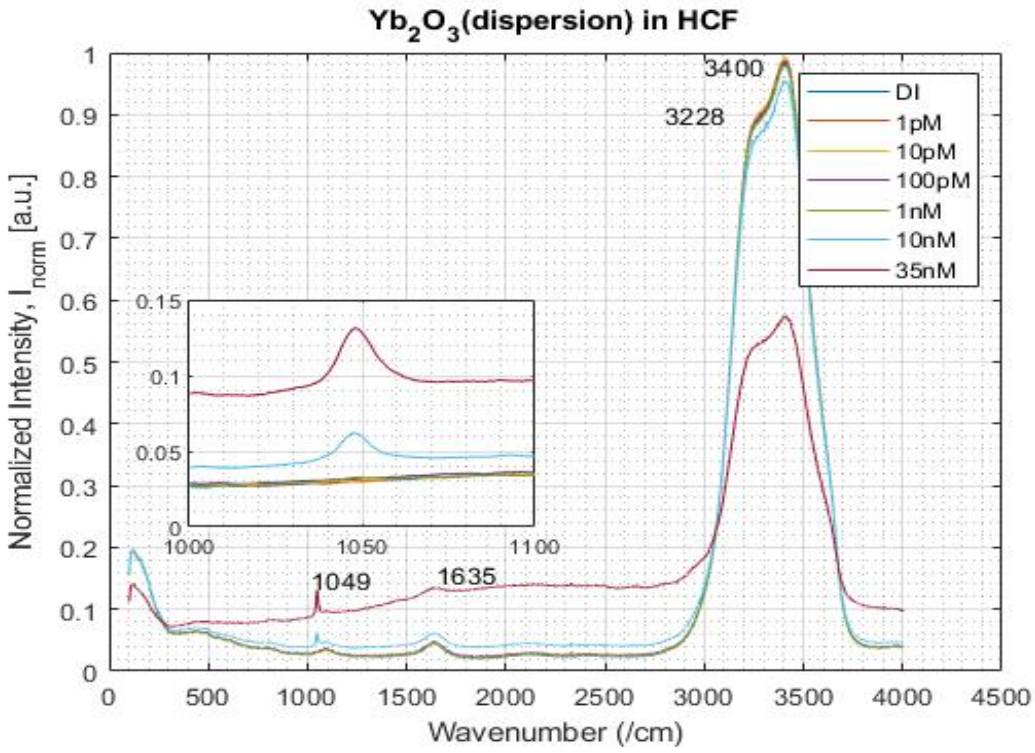

Figure 4.8: Normalized Raman for graded concentrations of Yb_2O_3 dispersion at 532nm

of DD water at 3400cm^{-1} [61]. This peak represents the anti-asymmetric stretching O-H bond in the water(H_2O) molecule. In contrast the peak at 3228^{-1} is due to the symmetric stretch of O-H bond. The peak at 1635cm^{-1} corresponds to the H-O-H structure of water(H_2O) molecule [61]. However a significant peak at 1049^{-1} is observed at higher concentrations of Yb_2O_3 suspension. A pattern of decreasing intensity of H_2O is seen with the increase of the concentration of Yb_2O_3.

For further investigation, Raman data is recorded on the residue of Yb_2O_3 obtained as a result of procedure explained in section 4.4.3. For this measurement, static scan is recorded unlike the previous measurements which are extended scans. With the static scan centered at 700cm^{-1} recordings are taken. With the measurements of the Yb_2O_3 the powder form on the microscopic glass slide, all the peaks of Yb_2O_3 are clearly observed. The plot indicating peaks of obtained for powdered form of Yb_2O_3 is shown in the Fig. 4.9. The most intense peak at 365cm^{-1} and 300cm^{-1},669cm^{-1} are pure Raman for Yb_2O_3 [62][63][64]. However the intensities of the peaks tend to change with the varying pressure and it's phase [65]. Analysis on these modes are beyond the scope of the thesis as the research is about identification

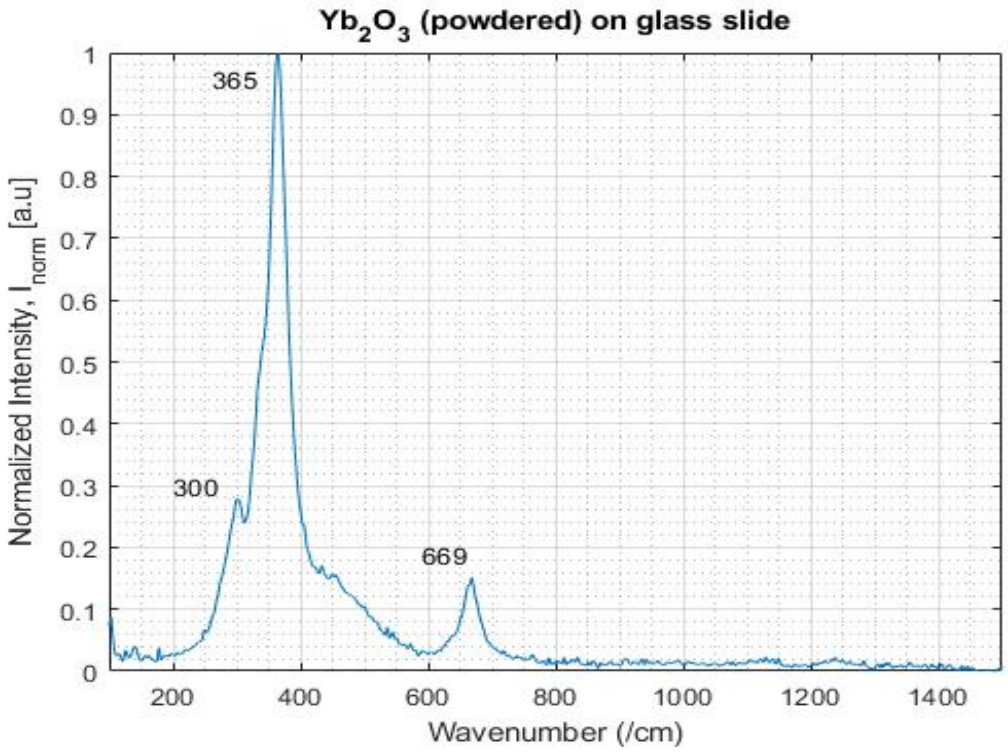

Figure 4.9: Normalized Raman spectra on Yb_2O_3 film at 532nm

of the elements and their proportions.

4.5 Raman Spectroscopy: H_2S Water

4.5.1 Hydrogen Sulfide: Background

Hydrogen Sulfide is a colorless, highly flammable gas with a particular odour of rotten eggs [66] [67]. It occurs naturally in the environment or by human activities. In nature it is produced due to the reduction of sulfates and sulfur containing organic/inorganic compounds. H_2S in large amount is present mostly in crude petroleum, volcanic gasses, natural gasses etc and trace quantities can be found in the underground water as a resultant of absorption from stagnant damp polluted waters/manure. According to the World Health Organisation (WHO), when large amounts of H_2S is released, it blocks the sense of smell [66]. Due to its highly flammable nature, it is susceptible to explode. Hence it is dangerous for the drilling personal in the oil and gas industry [67][68]. When H_2S is released into water, it causes irreparable damage to the marine life [69]. Therefore, it is very much important to be able to detect the presence of

H_2S in both gaseous and aqueous form. We identify the aqueous form of H_2S at the lowest concentration possible using Raman spectroscopy.

4.5.2 Procedure

All the samples used in this procedure were prepared right before the spectroscopy is done. This is due to, the natural existence of H_2S is in gaseous state. Since the samples used in this thesis are gas-saturated solutions in deionized distilled water, the H_2S tends to evaporate from the solution quickly [70] and settle back into its original gaseous form. Hence, spectroscopy was done immediately after the samples were prepared. The procedure in section 4.4.2 was followed by starting the measurements with DD water followed by increasing concentrations of aqueous H_2S up to its original concentration of lab sample i.e 117.3mM and the parameters of the Renishaw systems fixed to the extended scan similar to the measurements taken as in section 4.4.2.

4.5.3 Raman Spectra of Aqueous H_2S

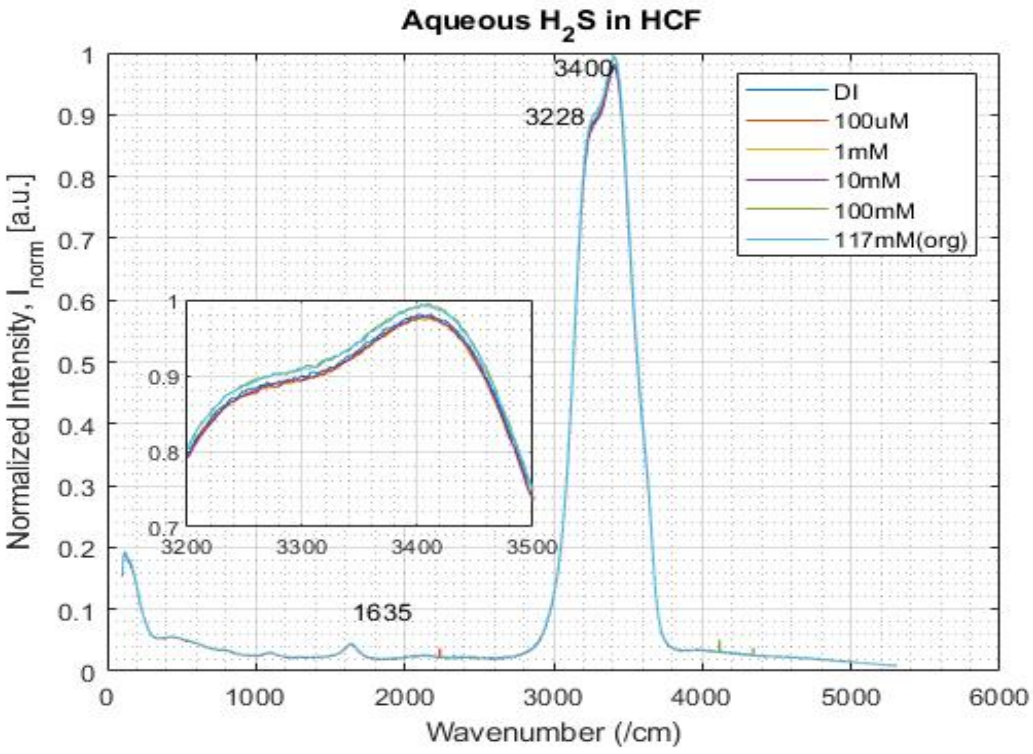

Figure 4.10: Normalized Raman spectra for aqueous H_2S at 532nm.

From the Fig. 4.10, we can observe that the spectra of H_2O and H_2S solutions have almost the same spectra and the characteristic peak is at $\simeq$ 3400 cm^{-1} that coincides with the experimentally measured vibrational frequencies [71] at 3490 cm^{-1}(asymmetric stretch of O-H), 3280 cm^{-1}(symmetric stretch O-H), and 1644 cm^{-1}(structure of molecule-same for H_2S and H_2O) respectively. This is attributed to the presence of relatively low level of H_2S in the solution with deionized distilled water. Hence the difference in their vibrational frequency is about 21-90 cm^{-1} with the characteristic peak width of 100-500 cm^{-1} [72][73]. The frequency detection range [72] of Raman spectroscopy is

$$R = \frac{f_B - f_A}{0.5(\omega_B + \omega_A)} \tag{4.7}$$

where f_A: frequency of the characteristic peak A,
f_B: frequency of the characteristic peak B,
ω_A: width of the characteristic peak A,
ω_B: width of the characteristic peak B
The calculated range of R from the data in the Fig. 4.9 is 0.146 to 0.21. This implies peaks of H_2S and H_2O have a large overlap, and are not distinguishable by Raman spectroscopy. However, an increase of the H_2S concentration could possibly define the difference but this is not desired because our purpose is to be able to identify low concentration of H_2S in an aqueous solution.

4.6 Raman Spectroscopy of Aqueous H_2S with CNT

4.6.1 Carbon Nanotubes: Background

Carbon nanotubes (CNT) have gained scientific attraction upon its discovery in 1991 [74]. There are two types of Carbon Nanotubes. A single-wall carbon nanotube (SWCNT) is a graphite layer twisted in a cylinder shape with diameter range of a nanometer, and multi-wall carbon nanotubes (MWCNT) are concentric cylindrical tubes [74][75][2] with the diameters of ranging up to few hundred nanometers. The structures of SWCNT and MWCNT are shown in Fig. 4.11 [76]. An ideal CNT offers the advantage of being light, flexible, anti-stress and thermally stable. The CNTs used in this research are Double Walled Carbon Nanotubes(DWCNT) from Sigma Aldrich with a diameter of 1.75nm. The concentration calculation of DWCNT is

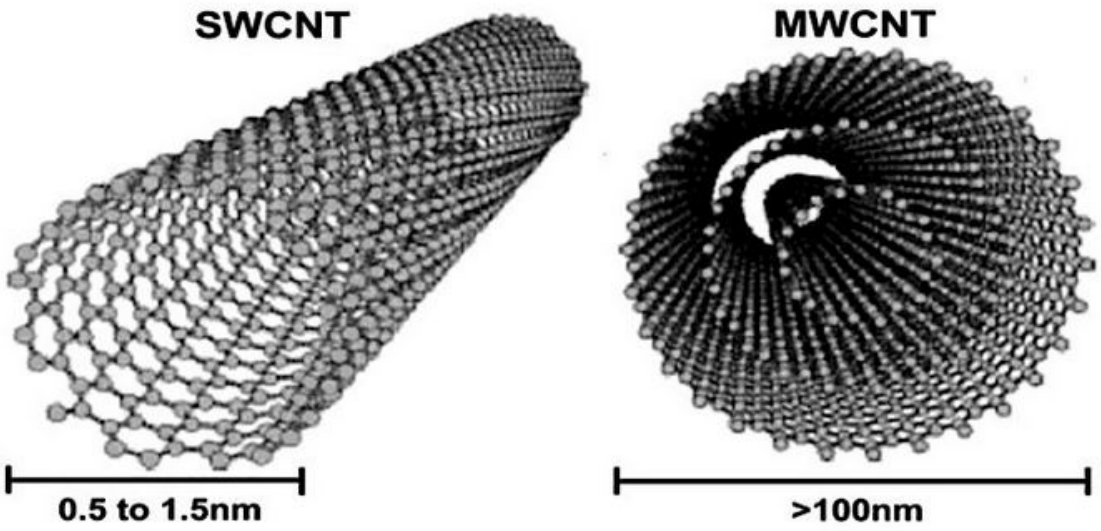

Figure 4.11: Single walled carbon nanotubes and multi walled carbon nanotubes. [2]

derived in the section 3.0.3.

4.6.2 CNT and its Relevance to H_2S Measurement

Using carbon nanotube as a medium to measure aqueous H_2S is based on the its adsorption property used in treatment and purification [72] in waste water treatment plants.

Adsorption

Adsorption is a process that migrates a molecule from a aqueous solution onto a solid surface. Reasons behind this mechanism can be either physical forces or chemical bonds of the adsorbing material. Adsorption is generally reversible called as desorption. This process is often described to measure the quantity of the element attached onto the surface of the adorbing material given the concentration in the liquid.

The pore structure of CNTs is the main factor causing reverse adsorption of H_2S. On the other hand, irreversible adsorption of H_2S is mainly due to chemical reactions. H_2S reacts with oxygen at low temperatures to form sulfur in the presence of activated carbon and water. The surface area tends to increase with an increase in the irreversible H_2S. Since CNTs have comparatively larger surface area and fine pore distribution, it makes an ideal material for H_2S adsorption. Using this property

of activated carbon, a mechanism which allows the adsoprtion of H_2S onto CNT is proposed by [72]. When CNTs are mixed into H_2S solution, a thin water film on the surface of the CNT is formed. Oxygen dissolved in the thin film behave as reactive points. H_2S molecules reaching the CNT gets dissolved in the formed thin layer of film and is partially dissociated as hydrosulfide ions (HS^-) and protons(H^+). The dissociated hydrosulfide ions undergoe a reaction with the Oxygen(O_2) molecule from water forming Sulphur(S) and hydroxyl ions(OH^-) where sulfur gets attached to the CNT [72] [77]. The hydroxyl ions(OH^-) gets neutralised by the protons (H^+) forming water as follows:

$$H_2S \rightarrow H^+ + HS^- \tag{4.8}$$

$$HS^- + 1/2O_2 \rightarrow S + OH^- \tag{4.9}$$

$$OH^- + H^+ \rightarrow H_2O \tag{4.10}$$

The main objective of using Carbon Nanotubes is to confirm if Raman is sensitive to H_2S in the presence of CNT.

4.6.3 Procedure

Three sets of data were recorded for H_2S in the presence of DWCNT. The measurement procedures are as follows,

- **Raman spectrum of DWCNT(nano powder):** This is done by carefully spraying the surface of a microscopic glass slide with 2.5mg of DWCNT, evenly spread like a thin film. The DWCNT film surface is then covered with a glass cover of 0.16mm thickness as shown in the Fig. 4.12.a, which is placed onto the stage of the Raman Microscope Raman microscope is operated at the wavelength of 532nm and 633nm with the exposure time of 10s and setting the power of the laser to 50% and is scanned for three times at approximately 120 seconds of each scan time.

- **Raman spectrum of DWCNT with H_2S spread on glass slide:** Recordings are taken at the same focal point by carefully dropping the graded concentrations of H_2S between the glass cover and the microscopic glass slide where the DWCNT layer. The Raman microscope parameters are same as previous measurements. The H_2S sample is made to contact the DWCNT layer thoroughly.

Figure 4.12: a)2.5mg of DWCNT nanopowder on a microscopic glass slide covered by a thin cover glass, b) Glass slide with DWCNT placed on the stage of Raman microscope foused with the laser beam of 532nm

- **Raman spectrum of DWCNT and H_2S suspension in core of HCF:** The last set of data is recorded for concentrations of H_2S prepared using 10nM of DWCNT suspension as explained in the 3.0.4. The samples are injected into the core of HCF similar to the procedure detailed 4.4.3 starting from DD water through the original concentration(117.3mM) of 10nM suspension of H_2S.

4.6.4 Results

DWCNT on microscopic glass slide

The Raman spectroscopy shown in Fig. 4.13 of the DWCNT, observes characteristic peaks which proves it be an effective method to identify the characterizations of CNTs. The main Raman peaks in the spectra obtained in any type of CNTs are located at $\simeq$1680 cm^{-1}(G-band), $\simeq$2700 cm^{-1}(2D-band), $\simeq$1360 cm^{-1}(D-band) [78][79][80][81]. The G-band is attributed to the characteristic feature of the pure graphite layer i.e. C-C bond and is directly related to the quality of the CNT. The D-band originates from the structural defects referred to as defect band whose intensity is relative to the G-band [78][79]. The more prominent D-band, indicates the structural defects in the CNT. Hence, the ratio of G and D bands represents the structural quality of CNT where higher qaulity CNTs have a ratio greater than 100. Intensity and the band shape of the 2D band amount to the number of graphite layers in the MWCNT. However, this band tends to fade with the increase of the layers [78][79].

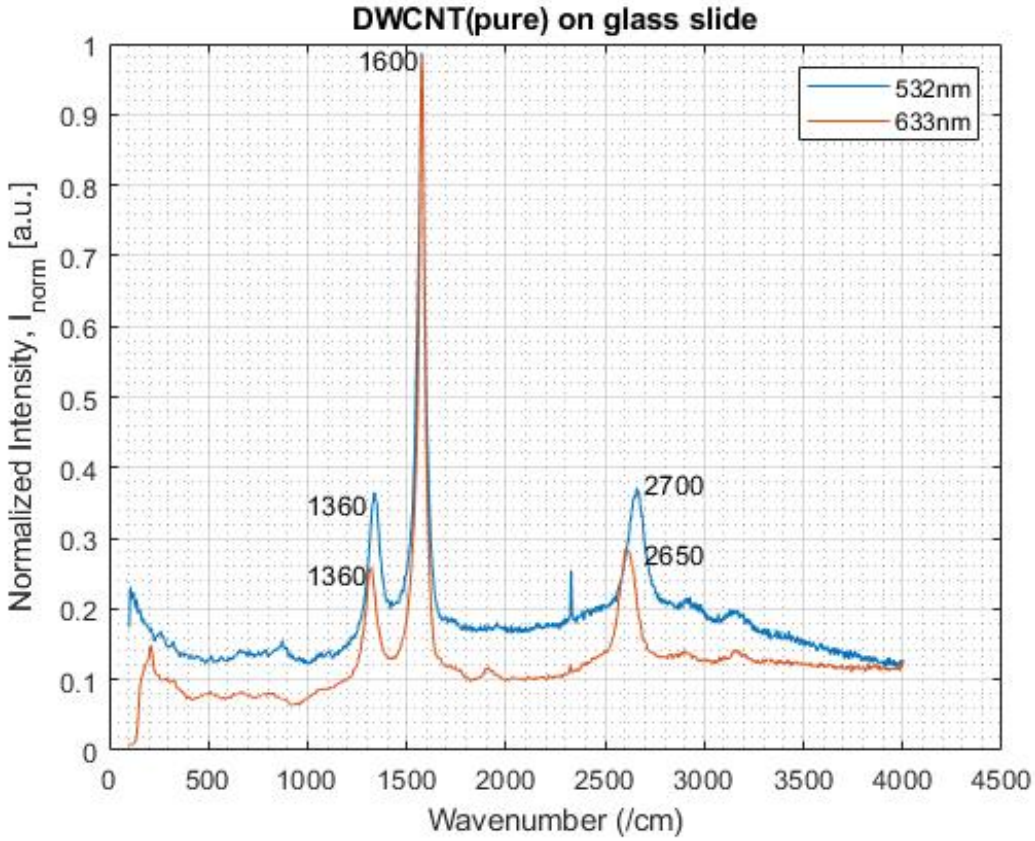

Figure 4.13: Normalized Raman spectra of DWCNT layer on glass slide at both 532nm and 633nm

DWCNT with H_2S on microscopic glass slide

The Raman spectra obtained for different concentrations of H_2S through the layer of DWCNT is plotted in Fig. 4.14. It is observed that the intensity increases with an increase in the concentration of H_2S. This validates the adsoprtion property of DWCNT with H_2S molecules. Fig. 4.15 is a zoomed in image of normalized Raman spectra of DWCNT with H_2S on glass slide on the x-axis range of 1200cm^{-1} to 2800cm^{-1}. The indicates a logical result that the intensity increases proportionally with the increase of the concentration[72][73]. From the plot in 4.15, identification of H_2S seems possible in the presence of Carbon Nanotubes. The key to the success of this method is to have uniform CNTs with less or no d-band($\simeq 1360 cm^{-1}$).

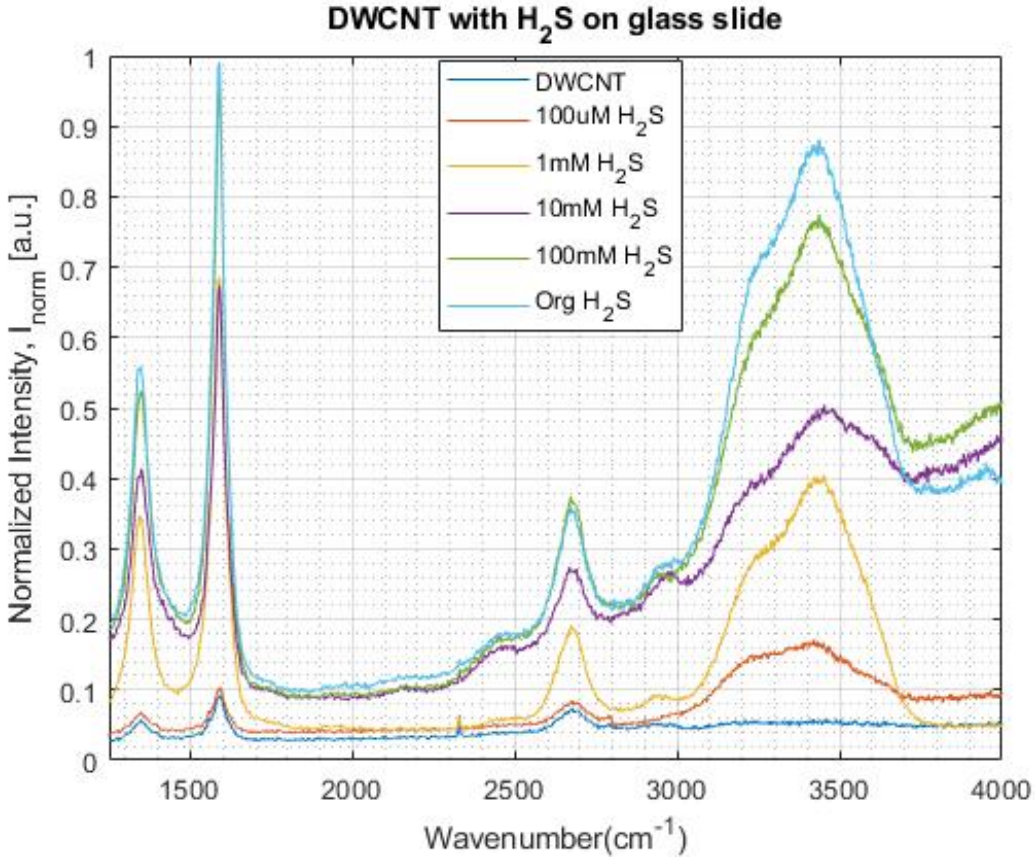

Figure 4.14: Normalized Raman spectra of DWCNT spread over a glass slide surface with introducing increasing concentrations of aqueous H_2S onto the DWCNT layer at the operating wavelength of 532nm

CNT with H_2S in the Hollow Core Fiber

Samples prepared as explained in the section 3.0.4 are passed into the hollow fiber in the graded order starting from distilled deionised H_2O as blank group, then 10nM of CNT suspension, 1μM H_2S in a 10nM DWCNT suspension, 10μM H_2S in a 10nM DWCNT suspension, 100μM H_2S in a 10nM DWCNT suspension, 1mM H_2S in a 10nM DWCNT suspension, 10mM H_2S in a 10nM DWCNT suspension, 100mM H_2S in a 10nM DWCNT suspension, 117.3mM H_2S in a 10nM DWCNT suspension. The spectrum obtained is shown in the Fig. 4.16. The spectrum at 1200cm^{-1} to 1800cm^{-1} observes a characteristic rise in the intensity with the increase in the concentration of H_2S. The results obtained in both the experiments to discriminate the concentrations H_2S in the presence of DWCNT is promising.

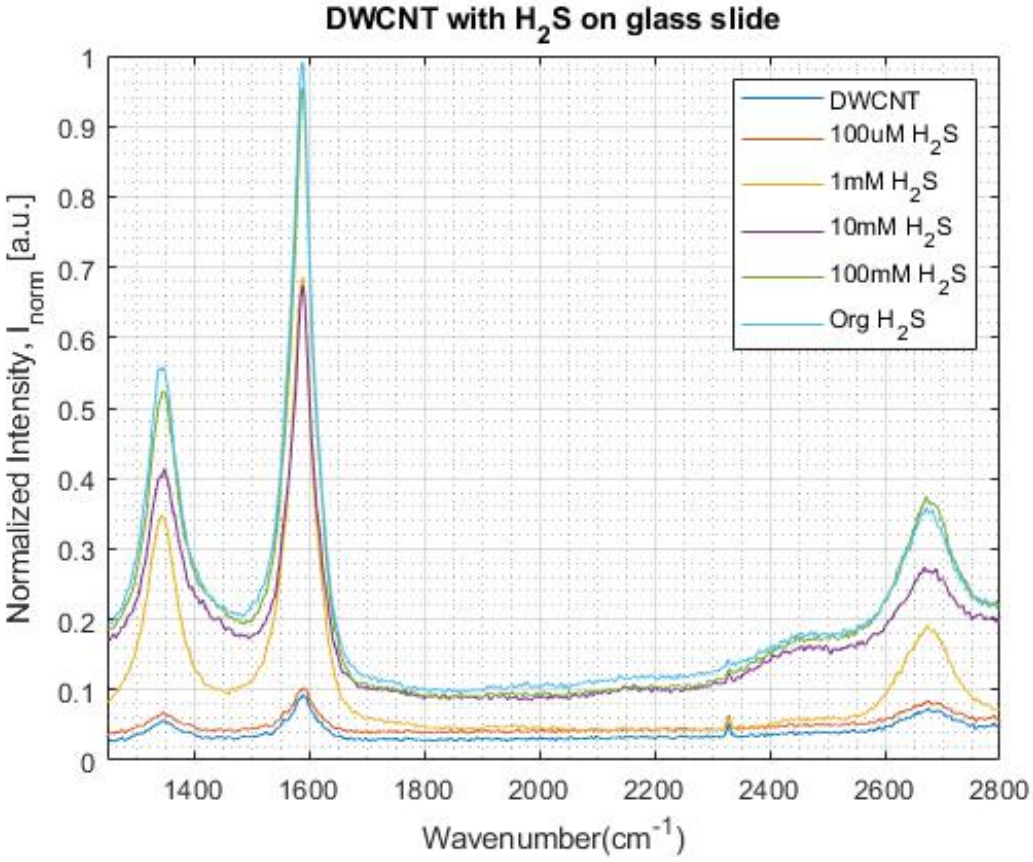

Figure 4.15: Expanded plot on wavenumber axis to view the increase in intensity

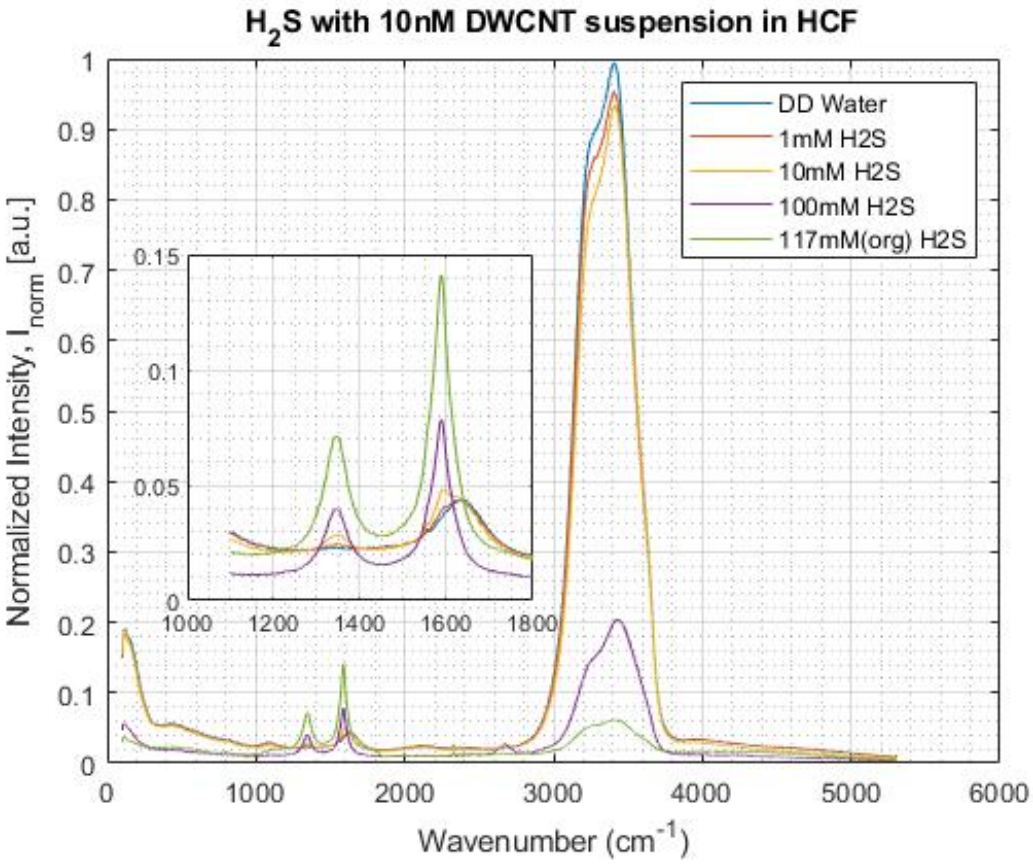

Figure 4.16: Normalized Raman spectra of increasing concentrations of aqueous H_2S in 10nM suspension of DWCNT passing through the HCF at operating wavelength of 532nm

Chapter 5

Analysis of Samples in a SCF-HCF Coupler

The SCF-HCF coupler is verified using Yb_2O_3 suspension, DWCNT suspension, H_2S solution, DWCNT, H_2S in DWCNT suspension. Changes in the intensity of the back reflections caused due to the different concentrations is studied to analyse the change in relation to the increase in concentration. As mentioned in Chapter 3, a USB4000 VS-NIR spectrometer from Ocean Optics is used to capture the change in the signal caused due to the interaction of sample with light at the coupling region. The spectrometer used is a USB device which can be connected to a PC to continuously monitor the change in intensity in real time using OceanView Software.

5.1 Raman Scattering and Fluorescence Emission in the Hollow Fiber Coupler

Raman scattering and Fluorescence are two parallel phenomenon that have similar origins. From the previous chapter, it is understood that when a laser source (λ_{exc}) strikes the molecule any one of the following processes can occur based on the structure and optical behaviour of the molecule. The excitation wavelength can lose a fraction of its energy thereby allowing the molecule to vibrate thus scattering at a wavelength greater than the excitation (Stokes) or scattering at a wavelength less than the excitation (anti-Stokes). The wavelength or frequency shifts of molecular vibrations of different molecules give rise to a spectrum which is specific to each element. On the other hand, fluorescence, phosphorescence or luminescence emission

follows absorption. In the process of fluorescence, the incident photon is absorbed by the molecule and is promoted to an excited state for a finite amount of time and jumps back to the ground state with emitting a photon at a larger wavelength than the incident wavelength. Fluorescence emission mostly occurs from the first excited state as the relaxation of the molecule from the higher excited state to the first excited state is quicker. Hence, it can be said that the fluorescence emission is independent of the incident wavelength and therefore the spectrum will not be shifted due to the change in the excitation wavelength. The results from the SCF-HCF coupler experiments are

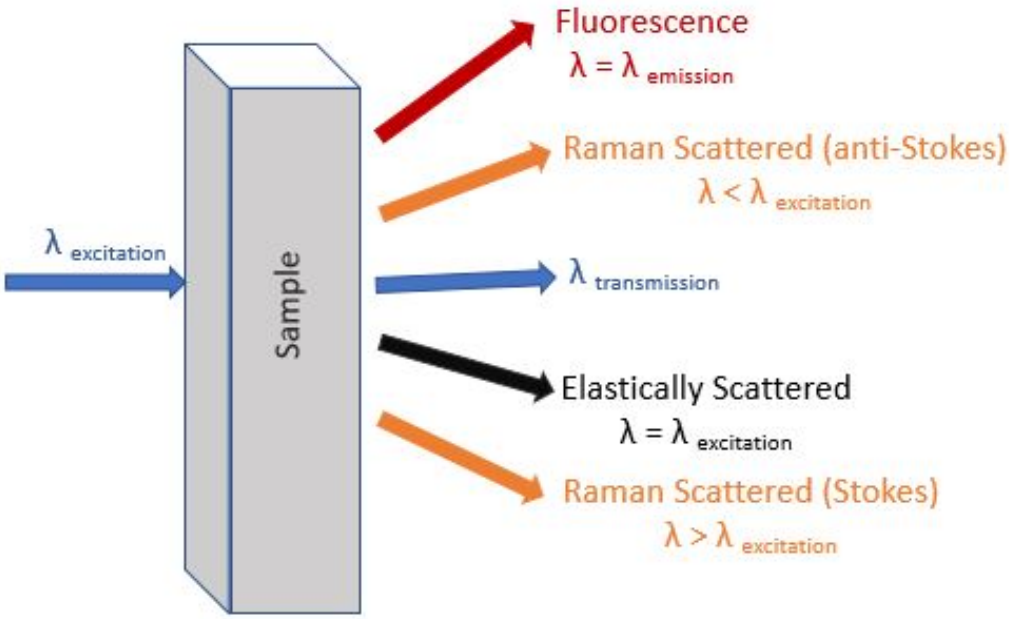

Figure 5.1: Fluorescence, elastic scattering and Raman scattering processes.

in reasonable agreement with the Raman anti-Stokes scattering and fluroscence emission. However due to the limitation of the spectrometer used in this thesis and the coupling efficiency of the coupler, it is identified that other process must be included to observe strong Raman signals which by nature are weak.

5.1.1 Characteristics of Absorption Spectroscopy

Absorption spectroscopy is the absorption of photons by electrons distributed within certain orbitals. Once, a photon is absorbed, an electron reaches a vacant upper orbit of higher energy thereby inducing molecule excitation. This process redistributes the electron cloud with the molecular orbits. This process is very rapid that there exists almost no time for the nuclei to move its position and hence the electronic transitions are always represented in vertical lines [82][83]. Therefore, the energy of a molecule is the sum of translational, rotational(molecular rotation around the gravity center), vibrational(periodic displacement of atoms from the equilibrium), electronic(movement of electron within the molecular bonds) and nuclear orientational spin energies. Absorption spectroscopy is higly sensitive to the temperature. An increase in the temperature would increase rotational and vibrational states of both the atoms and molecules and this changes the output signal [33]. Absorption spectrum is the plot of intensity as a function of wavelength. The intensity depends on the population of the atoms/molecules transitioning to the excited state. Hence the key is higher the population, the higher the intensity of the corresponding absorption spectra. However, measuring the absorption spectra of same element at different temperature would result in a modified signal.

5.1.2 Beer-Lambert's law

I_o: Input intensity of light entering sample
I_z: Intensity at some point z at the region of matter-light interaction

I: Output intensity of light after light-matter interaction
Total area of the cuvette where the sample is held is given by

$$A_{cuvette} = N\sigma dz A \tag{5.1}$$

Fraction of area where the light is absorbed is

$$\frac{dl}{I_z} = -N\sigma dz \tag{5.2}$$

where dl: Light intensity absorbed by the sample

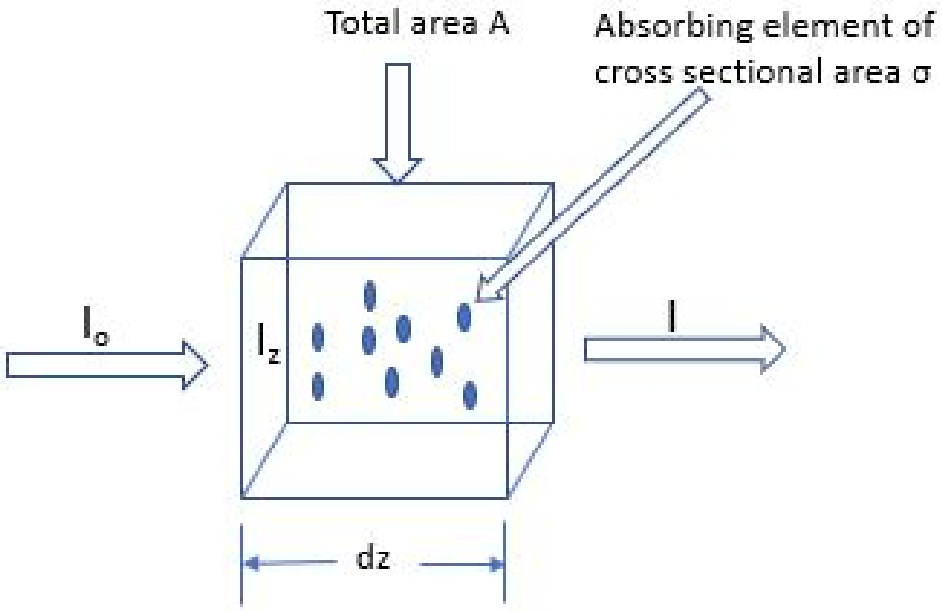

Figure 5.2: Beer-Lambert's law, deriving absorption

Integrating this equation from z = 0 to z = b, gives

$$\int_{z=0}^{z=b} \frac{dl}{I_z} = \int_{z=0}^{z=b} -N\sigma dz \tag{5.3}$$

$$ln(I) - ln(I_o) = -N\sigma b \tag{5.4}$$

$$ln\frac{I_o}{I} = N\sigma b \tag{5.5}$$

where N: molecules/cm^3 that is related to the concentration by

$\frac{N\times(1000cm^3/L)}{N_A} = c(M)$ and

2.303 $\times$ log(x) = ln(x)
Therefore,

$$log\frac{I_o}{I} = \frac{\sigma N_A cb}{2.303 \times 1000} \tag{5.6}$$

$$A = \epsilon bc \tag{5.7}$$

with

$$\epsilon = \frac{\sigma N_A}{2.303 \times 1000} \tag{5.8}$$

Transmittance is given by,

$$Transmittance(T) = \frac{I}{I_o} \tag{5.9}$$

$$\%T = 100T \tag{5.10}$$

Substituting 5.10 in 5.8,

$$A = \log_{10} \frac{I_o}{I} \tag{5.11}$$

$$A = 2 - \log_{10} \%T \tag{5.12}$$

Beer-Lambert's law is linear in most cases except

- at higher concentrations
- if the sample exhibits fluoresce or phosphoresce
- presence of stray light

5.2 Experiment Setup

5.2.1 Optical Components

The schematic diagram of the coupler experiment setup is shown in the following Fig. 5.3.

Light Source

Toptica tunable laser 815 nm to 855 nm high power(30 mW) is a used as a light source and its operating wavelength as determined to be 829.60nm using an Optical Spectrum Analyser(OSA) shown in Fig. 5.4.

2x2 Directional Coupler:

A 2×2 fiber optic coupler with a coupling ratio of 99:1 was used. The output from the Toptica laser source is connected to the the input of the coupler.

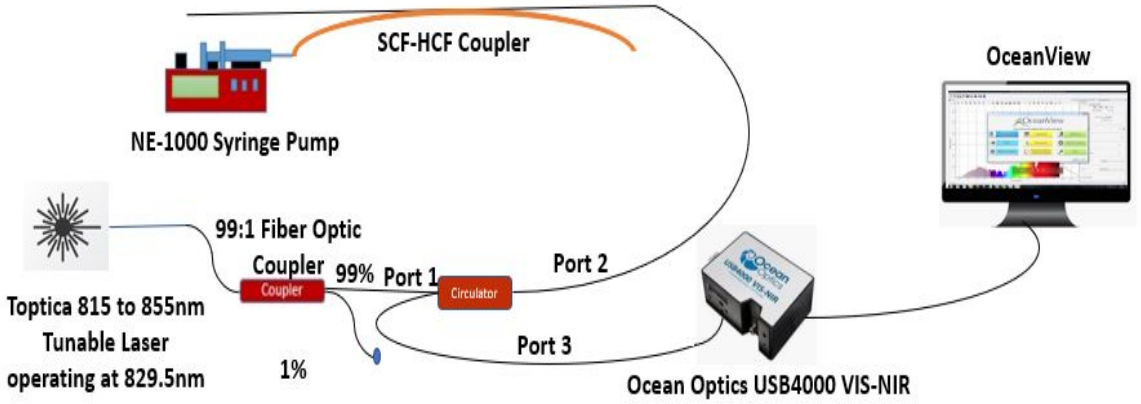

Figure 5.3: Schematic set up for the coupler experiments

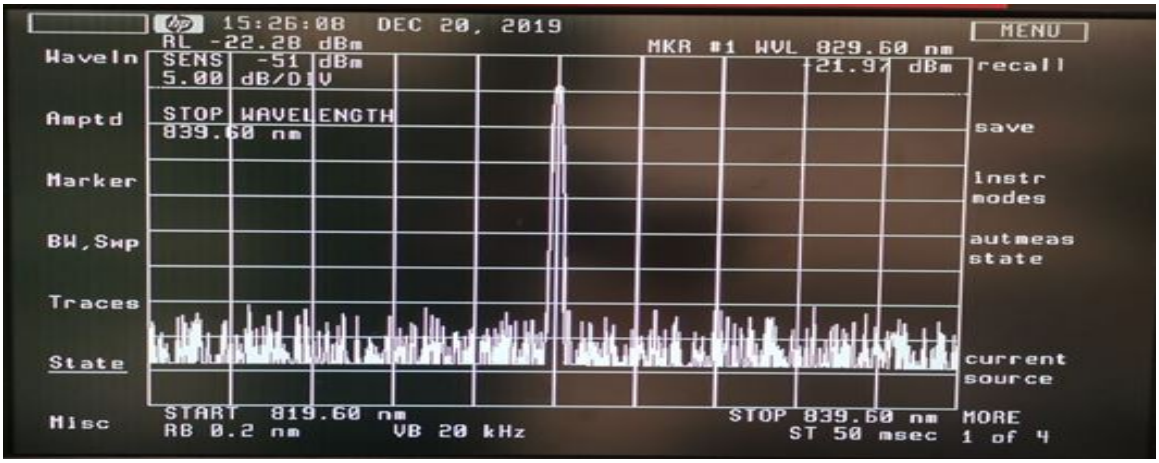

Figure 5.4: Determining the operating wavelength of Toptica tunable 815nm to 855nm laser using OSA to be 829.60nm

Optical Circulator(850nm):

It is a three-port device which allows light to travel only in one direction [84] unlike a directional coupler. The behaviour of an optical circulator is shown in the following Fig. 5.5. The signal entered into Port 1 exits through Port 2 with a very minimal loss. Similarly, the signal entering through Port 2 exits from Port 3 with minute loss. On the other hand light from port 2 to port 1 will experiences a large loss or no signal at port 1. Similarly, the light from port 3 experiences a large loss at ports 2 and 1. This feature makes them non-reciprocal devices which means that any changes occurred in the properties of the signal caused by passing through the circulator will not be reversed if travelled in the opposite direction. It is a high isolation and low

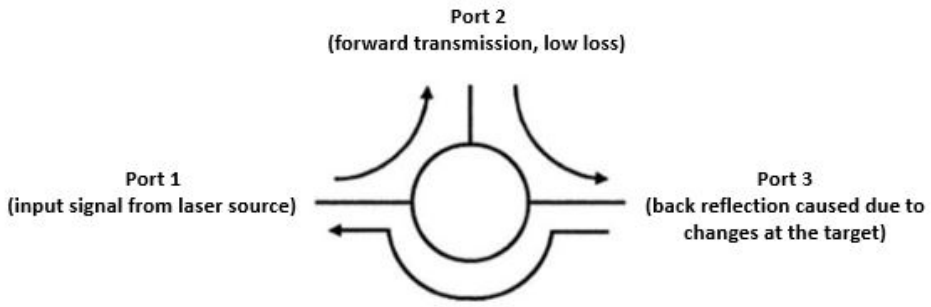

Figure 5.5: Conventional figure to represent the behavior of an optical circulator

insertion loss passive element in an optical network. An optical circulator is desired in this experiment because it can record the optical signals from a reflective device as explained later in this chapter.

Packaged Optical Hollow Fiber Coupler:

Port 2 of the optical circulator is connected to the SMF input port of the SCF-HCF coupler using an optical fiber connector. This connector aligns the core of port 2 of the circulator with the core of input port SC-HCF coupler, then mechanically couples the light from one to the other respectively so that the light can pass.

Syringe pump:

A regular 1ml syringe is driven by a NE 1000 programmable syringe pump. A needle(SurGuard® SG3-3013) is used to inject the sample into the hollow core fiber as shown in the Fig. 5.6. The sample was delivered at a rate of 0.1mL/minute into the hollow core fiber.

Ocean Optics Spectrometer:

Port 3 of the 850nm optical spectrometer was connected to the Oceanoptics USB4000 VIS-NIR photodetector. As mentioned in the previous section, Port 3 is connected to the spectrometer to measure the back reflection of the signal when the liquid sample is injected. Back reflections are recorded for each concentration, caused due to the

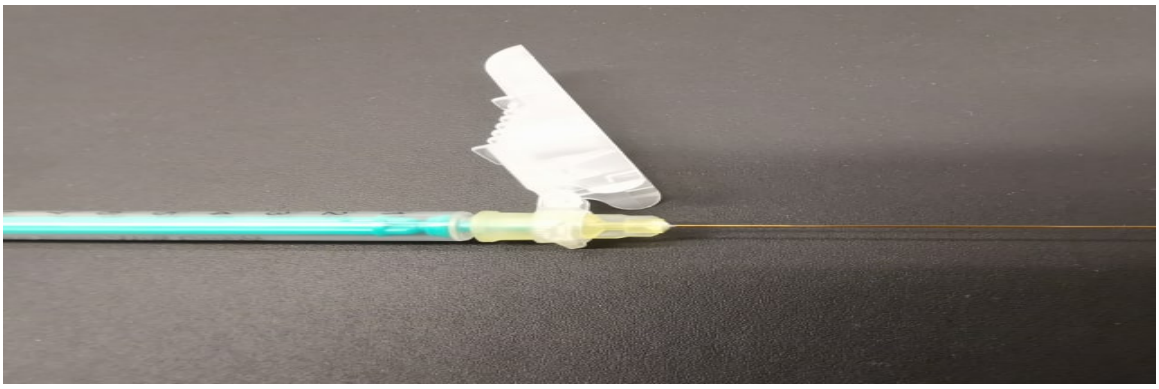

Figure 5.6: Insertion of needle into the core of HCF for sample injection

absorption or scattering of the input light signal upon the interaction of the input light with the test sample. USB4000 UV-VS-NIR is used to capture the output signal from the SCF-HCF coupler. OceanView software monitors and records the data of the interacted light. This spectrometer is good for visible light and a shorter Near Infrared wavelengths. The data transfer speed to the from the spectrometer to PC is every 5ms. The signal to noise ratio is 300:1 and hence very less noise interference to the desired signal

Ocean View Software:

Measurement techniques possible with the ocean view software are Absorption(based on concentration), Transmission, Reflectance, Raman, Fluorescence, Absolute Irradiance, Relative Irradiance, Photometry-Photons-Power-Energy, Color. However, the spectrometer used in the thesis is compatible to measure Absorption(based on concentration), Transmission, Reflectance, Fluorescence.

5.3 SCF-HCF coupler: Measurement Procedure of Samples

The output of the Toptica laser light source is connected to the silica core fiber input port of the 2x2 SCF-HCF coupler. The 99% port of the coupler is connected to the port 1 of the optical circulator. Port 3 is connected to the ocean optics spectrometer to monitor the absorption of the back reflections. The sample are passed from in the order of lowest to highest concentrations through the needle-syringe set driven by the

syringe pump. The diameter of the hollow core is 320μm and that of the needle is 300μm. This avoids leakages of the sample near the needle-fiber junction. It should be noted that the syringe needle set is changed for each concentration of the same and different samples to avoid contamination.

Step 1: The experiment set up is shown in the Fig. 5.3. The Toptica Tunable 815nm to 855nm laser is turned on 2 hours prior to the experiment. Port 3 of the circulator is connected to the spectrometer to record the back reflection.

Back Reflection

Back reflection is the light reflected back towards the source due to the reflections from the interface. In this thesis the interface relates to the sensing region of the SCF-HCF coupler. In recent times, back reflection is sought to be sensitive and recorded that can be analysed which carries information about the region responsible for reflection [85][86]. With the advent of the optical components such as circulator, measurement of back reflection has become possible and finds promising for optical sensors. This concept has been used to observe the changes in the signal with the change in the sample. This can be attributed to the principle of Rayleigh Scattering as shown in the Fig. 5.7. Rayleigh reflection due to back scattering is a property

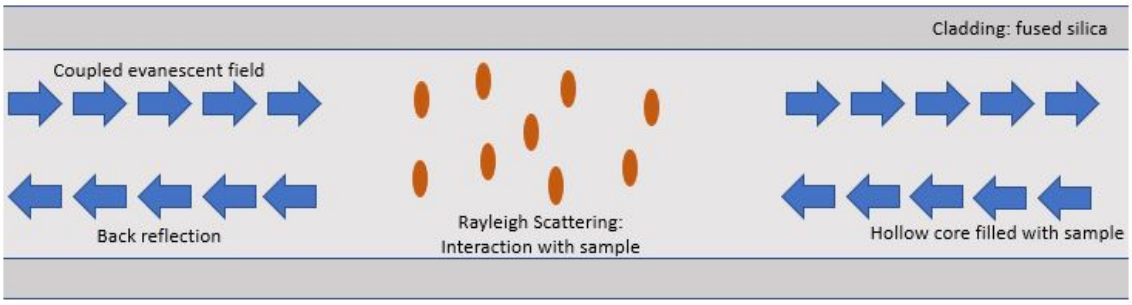

Figure 5.7: Rayleigh Scattering.

of optical fiber that is usually caused by defects or impurities introduced into the core of the optical fiber. A fraction of the scattered light directed back to the source. Port 3 of the optical circulator captures the reflections and are recorded using the OceanView software. In this context, an increase in the back reflection corresponds to the increase in the impurity and hence more scattering.

Step 2: The noise interference with the required signal is optimised by capturing the

Figure 5.8: Back reflection model.

signal with the laser source switched off and subtracting it with the signal obtained from the empty coupler. OceanView has a pre-configured procedure to complete this process, thereby avoiding manual submission.

Step 3: A needle is inserted on one end of the hollow fiber from the SCF-HCF coupler. The needle syringe set is driven by the programmable syringe pump(NE-1000) as shown in Fig. 5.6

Step 4: Samples are then injected into the coupler through the pre-programmed syringe needle set to regulate the flow, starting from the DD water as blank group through ascending order of concentrations to the highest available concentration in the lab.

Step 5: 100 measurements are recorded for each sample and the plots are the average of these measurements.

5.4 Results

The samples used in this thesis are graded concentrations of Yb_2O_3, DWCNT suspension, aqueous H_2S, DWCNT with H_2S suspension. The results obtained are promising and clearly elevates the sensitivity of the SCF-HCF coupler. From, the data obtained it can be understood that the back reflections are sensitive to different concentrations of a sample. Hence SCF-HCF coupler can be described as a reliable and cost effective device to help record the back reflections which have the higher SNR compared to

the measurements from the forward transmission.

5.4.1 Spectrum of Deionised Distilled Water at $\lambda_{exc} = 829.60$nm

Fig. 5.8 shows the spectrum obtained from an empty SCF-HCF i.e with no sample in the core of the hollow fiber and the spectrum with deionised distilled water filled in the core. As mentioned in the experiment procedure, both the measurements, the empty core coupler and the water filled core coupler is recorded for 100 times and are plotted as their average with the wavenumber(/cm) on the x-axis and normalized intensity on the y-axis. The back-scattered excitation wavelength at 829.60nm is also visible and though it exceeds the maximum of the y-axis, it did not saturate the spectrometer and hence had no influence in the recorded spectrum.

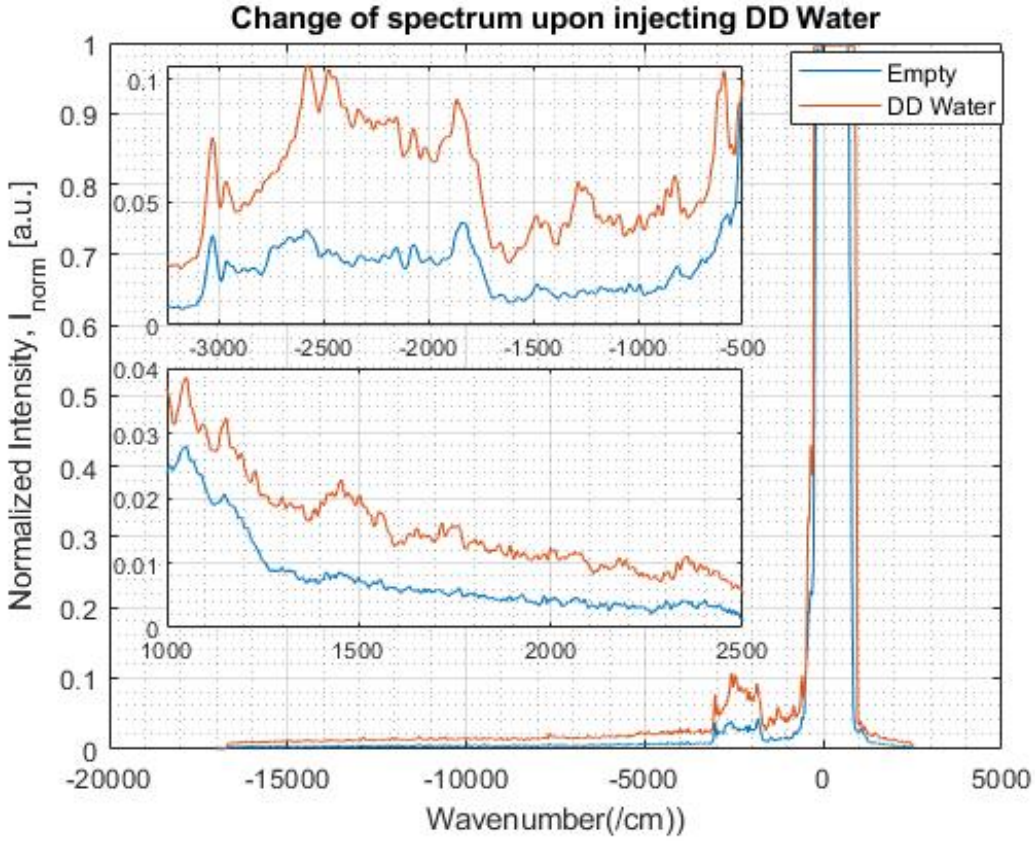

Figure 5.9: Spectrum of the empty and water filled SCF-HCF coupler

Both the insets in the Fig. 5.9 shows the enlarged spectrum obtained on the either sides of the excitation wavelength. The top inset shows spectrum obtained as a result

of the anti-Stokes Raman scattering where $\lambda < \lambda_{excitation}$ and the bottom inset of the Fig. 5.9 represents the Stokes Raman scattering where $\lambda > \lambda_{excitation}$. A significant increase in the intensity is observed uopn injection of the DD water. In general, with the increase in the particle size($\geq \lambda/10$), the scattering pattern moves to forward (transmitted) direction and lesser in the backward (reflected) direction. Since, the size of the water molecule is very small compared to the laser excitation source which is 829.60nm in the experiments, there exists more of the back scattering as observed in the Fig. 5.9.

5.4.2 Analysis of Yb_2O_3 Suspension in SCF-HCF Coupler

As mentioned in the procedure, samples are injected into the core of the SCF-HCF coupler in the order of Deionised Distilled(DD) water, 1pM, 10pM, 100pM, 1nM, 10nM concentrations of Yb_2O_3 suspension. The concentration of the original sample available in the research facility is 35nM suspension. However, when tried to inject the 35nM concentration of Yb_2O_3,it clogged the pathway of the liquid channel i.e the core of HCF. Hence, the measurements are taken for Yb_2O_3 concentrations up to 10nM.

It is observed from Fig. 5.10 that there is a change in intensity of spectrum in the increasing pattern upon injection of Yb_2O_3 suspension. The increase in intensity is attributed to the increase in the concentration of the Yb_2O_3 suspension. With the increase in the concentration of the nanoparticles, the incident light i.e. the light at 829.60nm gets more scattered resulting in the increase in the intensity. From [87], the intensity of the light scattered is directly proportional to the radius of the particle and inversely proportional to the excitation wavelength and is given by:

$$I_{scattered} \quad \alpha \quad \frac{r^6}{\lambda_{exc}^4} \qquad for \quad r < \lambda \tag{5.13}$$

$$I_{scattered} \quad \alpha \quad \frac{r^4}{\lambda_{exc}^2} \qquad for \quad r \approx \lambda \tag{5.14}$$

$$I_{scattered} \quad \alpha \quad r^2 \qquad for \quad r > \lambda \tag{5.15}$$

The above equations are valid for particle sizes comparable to the excitation wavelength. In case of extreme larger particles, factors such as the nature of the surface, refractive index are more influential on light scattered than the excitation wavelength.

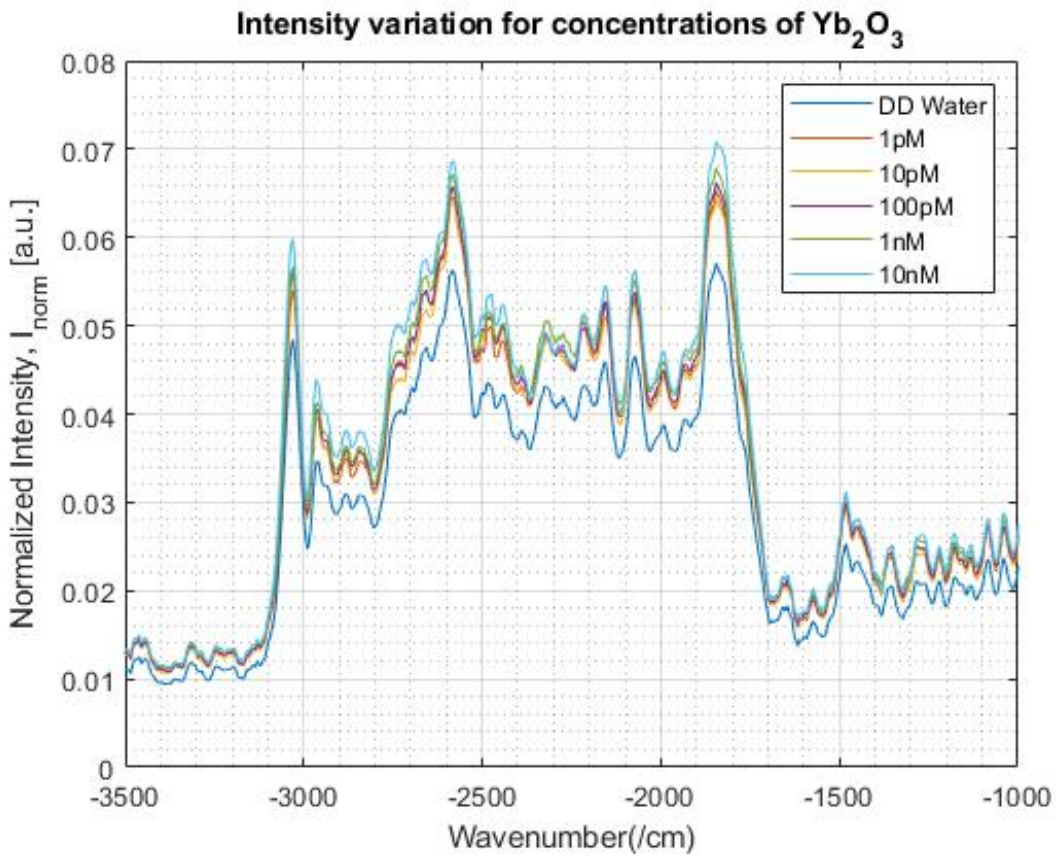

Figure 5.10: Normalised intensity of the spectrum for graded concentrations of Yb_2O_3 in the region of $\lambda < \lambda_{excitation}$

Fig. 5.11 shows the spectrum of the Stokes scattering where $\lambda > \lambda_{excitation}$ i.e. the wavelength of the emitted light is greater than the excitation wavelength. Standard deviation plotted as error bars for the intensity across the concentrations of Yb_2O_3 is given in the Fig. 5.12 shows the increase in the intensity with the increase in the concentration.

5.4.3 Measurement of H_2S water

Procedure similar as described in Section 5.3 is followed to obtain the spectrum of the back reflections of each H_2S sample by injecting the samples from the lowest to the highest concentration. The data recorded for 100nM, 100uM, 1mM, 10m, 100mM, 117.3mM(original) concentrations is plotted in the Fig. 5.13.

Fig. 5.13 shows no significant change in the intensity of the spectrum with the change in the concentration of the sample introduced. It is observed that the spectrum

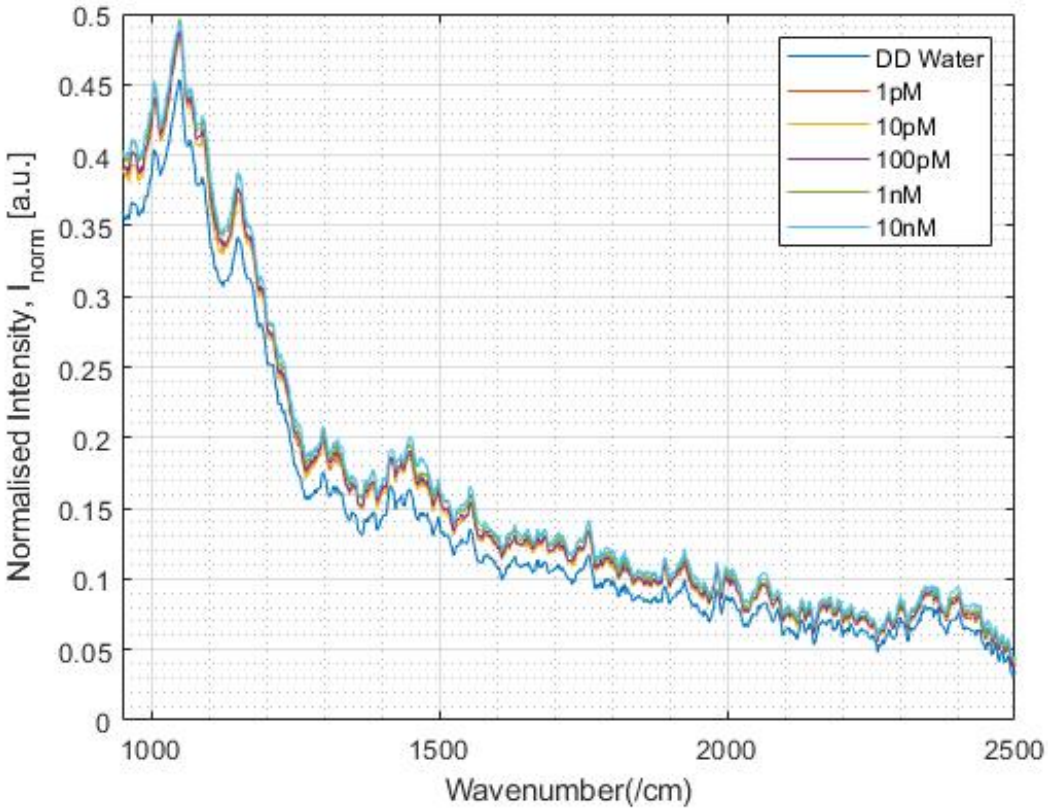

Figure 5.11: Normalised intensity of the spectrum for graded concentrations of Yb_2O_3 in the region of $\lambda > \lambda_{excitation}$

of the various concentrations of H_2S water almost overlap with each other and also with the deionised distilled water spectrum despite increase in their concentration except for the highest concentrations of H_2S which are 100mM and 117.3mM(original) samples. This pattern is attributed to the fact that the dimensions of both the DD water(H_2O) and H_2S molecule are almost same. The dimensions of both the molecules are given in the Fig. 5.14:

5.4.4 Measurement of DWCNT suspension

A procedure similar to the measurement of Yb_2O_3 suspension and aqueous H_2S is followed to obtain the spectrum and observe the changes for increasing concentrations of Double-walled carbon nanotubes suspensions in DD water. The data obtained is normalized as explained in the Section 4.3.3 and is plotted as shown in the Fig. 5.15.

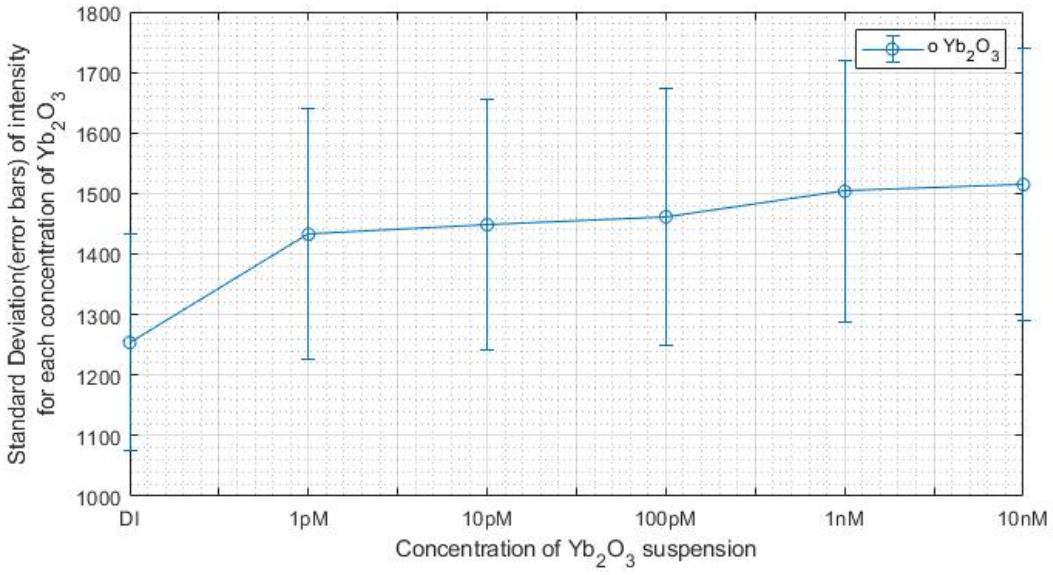

Figure 5.12: Standard Deviation(error bars) plotted against concentrations of Yb_2O_3 suspension

The plots of various concentrations of DWCNT dispersion overlap each other. It is also observed that there is a significant jump in the intensity of the back scattered light upon injecting the DWCNT dispersion after DD water. Apparently, after a series of measurements of DWCNT suspension in different couplers, a similar pattern is observed where the spectrum of different concentrations remained almost the same. [88] explains a similar inelastic scattering occurring in the carbon nanotubes suspension

5.4.5 Measurement of Aqueous H_2S in DWCNT Suspension

Samples of 100nM, 100μM, 1mM, 10mM, 100mM, 117.3mM (original) concentrations of aqueous H_2S in 10nM DWCNT suspension prepared as explained in Section 3.0.4 are injected into the core of the HCF in the SCF-HCF coupler. Data for each concentration in the ascending order was recorded in a procedure similar to the previous measurements. 10nM suspension of DWCNT is considered ideal for the coupler fabricated during this process. It is found that any concentration above 10nM DWCNT suspension blocks the coupling region of the SCF-HCF due to the core diameter at the coupling region being in the order of 100μm.

Fig. 5.16 is the average intensity of the spectrum as a function of time obtained

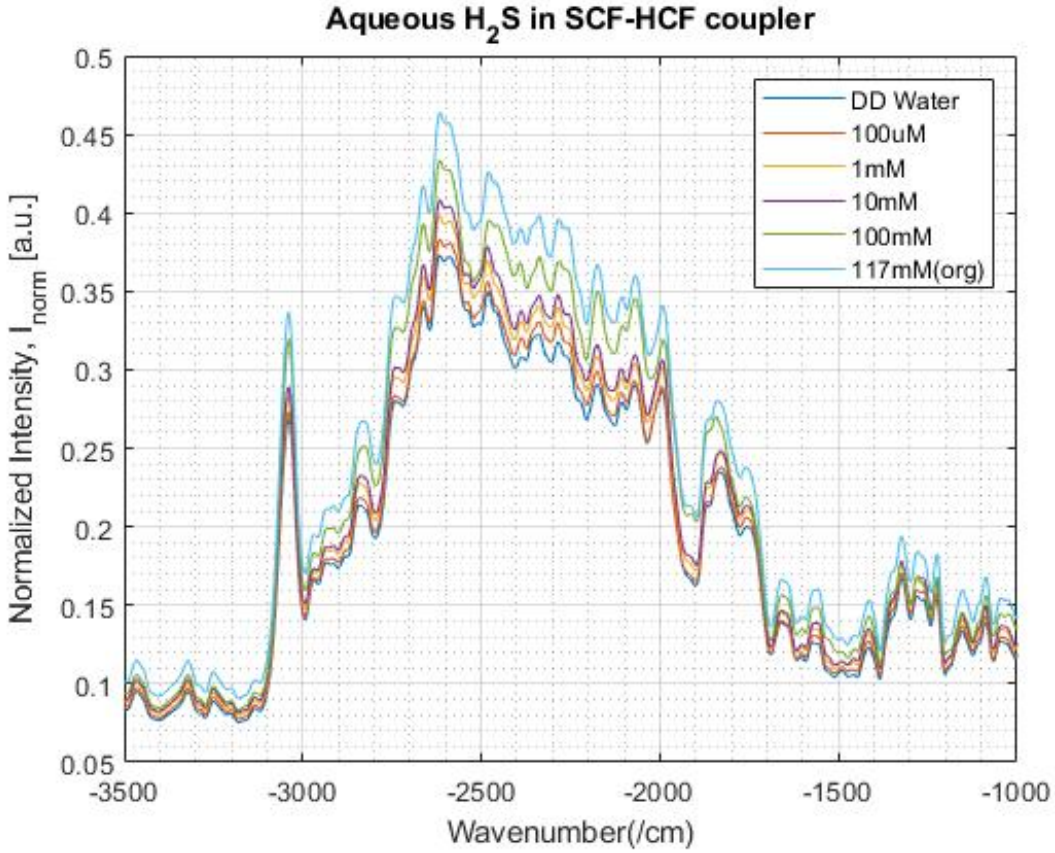

Figure 5.13: Normalised intensity of the spectrum for graded concentrations of aqueous H_2S in the region of $\lambda < \lambda_{excitation}$ where $\lambda_{excitation} = 829.60$nm

from the back reflections caused due to the light matter interaction at the coupling region for increasing concentrations of aqueous H_2S in 10nM DWCNT dispersion. The average intensity is observed to be increasing with the increasing concentrations of aqueous H_2S in DWCNT suspension. This is similar to the results obtained from Raman Spectroscopy of aqueous H_2S in DWCNT suspension in the stand alone HCF as described in the Section 4.6.5.

5.5 Comparing the Spectrum of all the Samples used

Fig. 5.17 shows the spectrum the highest concentration of the samples prepared. The comparison observes a significant change in the intensity of the reflected signal with different samples along with its shape.

	Bond length	Bond Angle
O-H	0.1375nm	104.5^o
S-H	0.1375nm	90^o

Figure 5.14: Bond dimensions of H_2O and H_2S molecule.

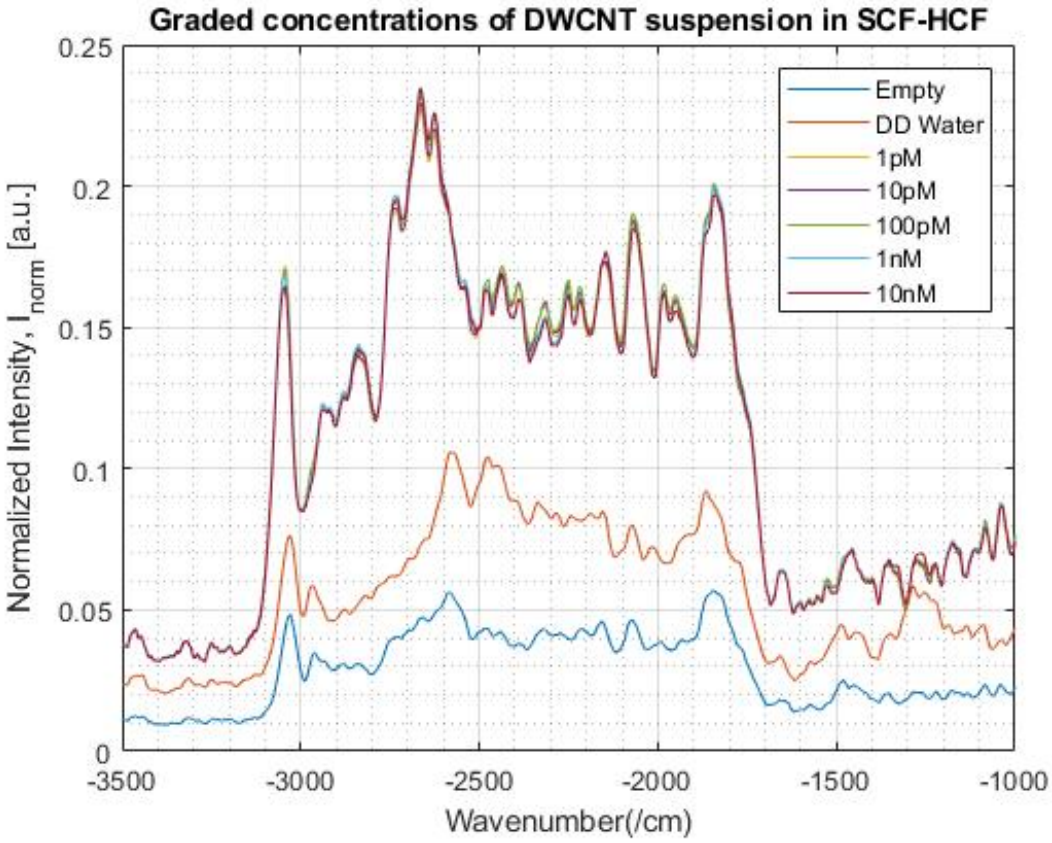

Figure 5.15: Normalised intensity of the spectrum for graded concentrations of DWCNT suspension in the region of $\lambda < \lambda_{excitation}$ where $\lambda_{excitation} = 829.60$nm.

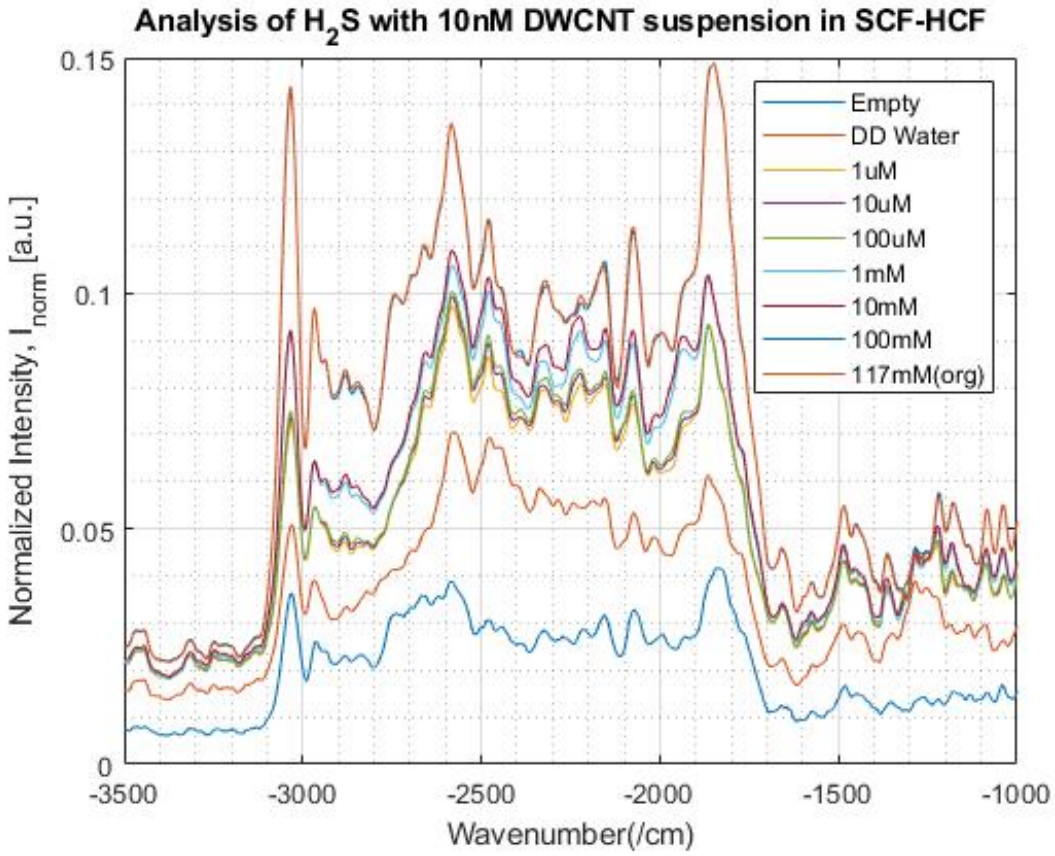

Figure 5.16: The average intensity across the spectrum over the entire period of experiment for H_2S in DWCNT suspension.

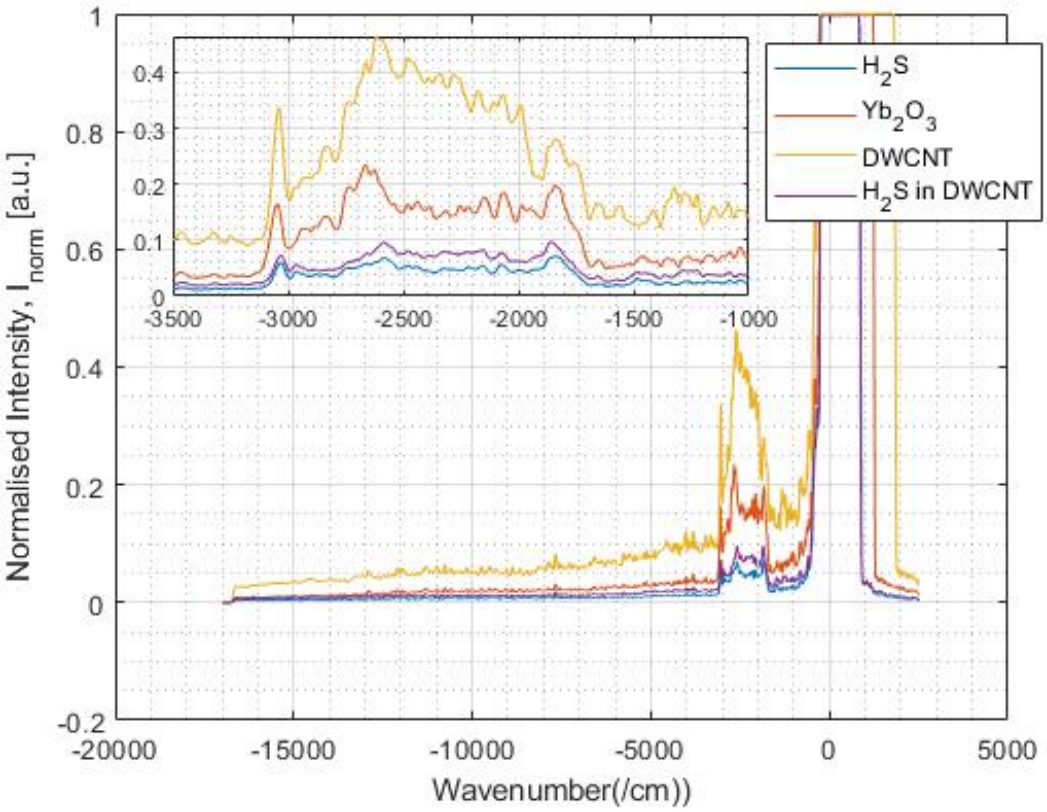

Figure 5.17: Normalised intensity spectrum comparison for the four different samples used in the thesis at the operating wavelength of 829.60nm.

Chapter 6

Conclusions and Future Work

6.1 Conclusions

In this research, four materials were proposed to perform Raman analysis for graded concentration of each material passing through the core of the HCF *case(i)* via traditional Raman Spectoscopy method and *case(ii)* signal obtained through the interaction of 829.60nm laser signal with the sample in the HCF at the coupling region in a SCF-HCF coupler. Both the cases are applied to identify the change in the intensity of the back reflections due to the change in the concentration of the sample introduced. Some salient points are concluded as follows:

1. Traditional Raman spectroscopy (Renishaw system at operating wavelength 532nm) of ordered concentrations of Yb_2O_3 suspension in the core of a stand alone HCF identifies missing the Raman peaks of Yb_2O_3. However, the intensity of the water peak is found to be decreasing with the increasing concentration of Yb_2O_3. To further investigate, Raman spectroscopy is performed on dried powdered form of Yb_2O_3 on a glass slide at the same operating wavelength of 532nm. The amorphous form of Yb_2O_3 displayed all the characteristic peaks of Raman. On the other hand, increase in the intensity of the back reflections w.r.t increase in the concentration of Yb_2O_3 is observed for the samples in the SCF-HCF coupler at 829.60nm guiding wavelength. Further verification of Raman analysis might produce the reasons for the missing peaks of Yb_2O_3 in aqueous environment within HCF. The techniques include, change of the focal point, performing Raman on HCF with lesser diameter.

2. Raman analysis of varying concentration of aqueous H_2S in a stand alone HCF

via traditional Raman method (operating wavelength 532nm) determine that the Raman peaks of H_2S and H_2O are not distinguishable i.e. both the the peaks overlap with the minor shift ranging between 21-73 cm^{-1}. This is attributed to the fact that the vibrational frequencies and the shape/orientation of molecules (H_2S and H_2O) are same . A similar pattern of overlapping spectrum of both DD water and aqueous H_2S is found in the data recorded using SCF-HCF coupler. This led to the study of CNTs and its importance in identifying H_2S in aqueous environment.

3. Raman spectroscopy with DWCNT spread as a thin film on a microscopic glass slide measured using the Renishaw system at the operating wavelength of 532nm identified all the D, G, 2D bands which are pure Raman for DWCNTs. All the typical peaks of the DWCNT are observed. From the peaks obtained, it is observed that the quality of the DWCNTs used are higher taking into consideration the ratio of the intensities of D and G bands to be greater than 100.

4. Applying the concept of waste water treatment with DWCNT to remove H_2S molecules, Raman spectroscopy is done with varying concentrations of H_2S in 10nM suspension of DWCNT in a stand alone HCF using the Renishaw system at 532nm. Due to the absolute adsorption properties of DWCNTs, increase in the intensity is observed with the increase in the concentration of H_2S which was not seen with concentrations of plain H_2S. Moreover, this is verified by performing Raman spectroscopy for same concentrations of H_2S solution by dropping the sample in the increasing concentrations onto the glass slide containing the layer of DWCNT on its surface. In both the cases, similar results are obtained. This proves that aqueous H_2S is identifiable even in the presence of DWCNTs in comparison to the published results of identifying aqueous H_2S using MWCNT.

5. No change in the intensity is observed with increasing concentrations of DWCNT suspension flowing through the core of SCF-HCF coupler. The intensity of the back reflections remained the same despite increase in the DWCNT concentration. However, a sudden increment in the intensity is observed from DD water to any concentration of DWCNT. On the other hand, an increasing pattern of intensity is observed for increasing concentrations of aqueous H_2S in a 10nM suspension of DWCNT.

6.2 Future Work

The future work includes fabricating a more compact, robust SCF-HCF with increased sensitivity and optimised cost. The sensitivity can be increased by etching the cladding of the hollow core fiber prior to pulling the coupler. This reduces the thickness of the cladding while the diameter of the core remaining same. This can be achieved by using various methods, for instance HF(Hydrogen Fluoride) can be used for regulated etching. Capillary effect can be applied to pass the sample through the coupling region of the SCF-HCF coupler. This could avoid the usage of syringe, needle and the syringe pump to drive the sample into the coupler. This drastically reduces the size of the SCF-HCF coupler system. The enclosed sensing region of the SCF-HCF coupler can be removed off the base glass slide which further reduces the size. Also, the huge sized laser sources can be replaced by photodiode.

Further research includes Raman analysis of the samples at the sensing region. This can be done by using the photodetector compatible to the read and display the Raman signals from the sample.

Bibliography

[1] J. E. Sipe, L. Poladian, and C. Martijn de Sterke, *Propagation through nonuniform grating structures.* Journal of the Optical Society of America, 1994, Vol. 11, 5668.

[2] A. Ahmad, M. Kholoud, A. Reda, and R. A.-W. Abdul, *Carbon nanotubes, science and technology part (I) structure, synthesis and characterisation.* Arabian Journal of Chemistry, 2012, Vol. 5, 1-23.

[3] G. A. Hockham and K. C. Kao, "Dielectric-fibre surface waveguides for optical frequencies," 1966.

[4] F. Hamid, W. Rahman, and N. H. Mohd, *Humidity sensors principle, mechanism, and fabrication technologies: as comprehensive review.* Sensors, 2014.

[5] A. D. Kersey, *A review of recent developments in fiber optic sensor technology.* Optical Fiber Technology, 1996, 291-317.

[6] P. Toni, *Fibre bragg gratings optical sensing technology.* Smart Materials Bulletin, 2001, 7-10.

[7] L. Byoungho, *Review of the present status of optical fiber sensors.* Optical Fiber Technology, 2003, 57-79.

[8] K. T. V. Grattan and T. Sun, *Fiber optic sensor technology: An overview.* Sensors and Actuators, 2000, 40-61.

[9] A. P. Mouritz, *23 - Nondestructive inspection and structural health monitoring of aerospace materials.* Introduction to Aerospace Materials, 2012, 534-557.

[10] H. Muhammad, R. Aran, S. Mustafa, and G. O. Abdul, *Properties of glass materials.* Reference Module in Materials Science and Materials Engineering, 2015.

[11] G. Kim, S. Park, and C. Park, *Real-time quasi-distributed fiber optic sensor based on resonance frequency mapping.* Springer Nature, Sci Rep 9, 2019.

[12] K. Fidanboylu, *Fiber optic sensors and their applications.* Chronicles of Young Scientists, 2019.

[13] K. O. Hill and G. Meltz, *Fiber bragg grating technology fundamentals and overview.* Journal of Lightwave Technology, 1997, Vol. 15, 1263-1276.

[14] G. Chiranjit, A. Quazi Md, and G. Biswajit, *Spectral characteristics of uniform fiber bragg grating with different grating length and refractive index variation.* International Journal of Innovative Research in Computer and Communication Engineering, 2015,Vol. 3, Issue 1.

[15] J. Chen, B. Liu, and H. Zhang, *Review of fiber bragg grating sensor technology. Front.* Optoelectronics, 2011, Vol. 4, 204-212.

[16] G. Tsigaridas, D. Polyzos, A. Ioannou, M. Fakis, and P. Persephonis, *Theoretical and experimental study of refractive index sensors based on etched fiber Bragg gratings.* Sensors and Actuators, 2014, Vol. 209, 9-15.

[17] R. S. K. Nidhi and P. Kapur, *Theoretical and experimental study of long-period grating refractive index sensor.* Fiber and Integrated Optics, 2014, Vol. 33, 37-46.

[18] V. Bhatia, *Optical fiber long-period grating sensors.* Optics Letters, 1996, Vol. 21, 692-694.

[19] I. Del Villar, M. Achaerandio, I. R. Matas, and F. J. Arregui, *Optimization of sensitivity in long period fiber gratings with overlay deposition.* Opt. Express, 2005, Vol.13, 5668.

[20] S. Somekh and M. Barnoski, *Optical directional couplers.* Introduction to Integrated Optics, Springer, 1974.

[21] Sudarsono, Y. Gatut, S. Hasto, P. Gontjang, A. Diky, P. Nurrisma, I. Susilo, F. Iim, Y. Ali R, and H. Yono, *Design and fabrication of optical waveguide as directional coupler using laser cutting CO_2 on acrylic substrate.* Journal of Physics: Conference Series, 2019, Vol. 1153.

[22] B. J. Luff, R. D. Harris, J. S. Wilkinson, R. Wilson, and D. J. Schiffrin, *Integrated optical directional coupler biosensor.* Optics Letters, 1996, Vol. 21, 618-620.

[23] W. Shin, S. Choi, and K. Oh, *All-fiber wavelength- and mode-selective coupler for optical interconnections.* Optical Society of America, 2002, Vol. 27.

[24] J. Liu, T. H. Cheng, Y. K. Yeo, Y. Wang, Z. Xu, and D. Wang, *Fused biconical tapered technique based light beam coupling between a single mode fiber and a high nonlinearly photonic crystal fiber.* Optical Society of America, 2009.

[25] H. Yokota, H. Yashima, Y. Imai, and Y. Yutaka Sasaki, *Coupling characteristics of fused optical fiber coupler formed with Single-mode fiber and photonic crystal fiber having air hole collapsed taper.* Advances in Opto Electronics, 2016.

[26] K. T. Kim, H. K. Kim, S. Hwangbo, S. Choi, H. B. Lee, and O. Kyunghwan, *Characterization of evanescent wave coupling in side-polished hollow optical fiber and its application as a broadband coupler.* Optics Communications, 2005, 145-151.

[27] J. C. Chen, C. W. Ho, and J. S. Wang, *Optical Fiber coupler with a hollow core fiber for magnetic fluid detection.* Lightwave Technology, 2012, Vol. 34, 5220-5225.

[28] H. Qu and M. Skorobogatiy, *Liquid-core low-refractive-index-contrast Bragg fiber sensor.* Applied Physics Letters, 2011, Vol. 98, 114-201.

[29] K. Zheng and L. Shang, *High-Linearity refractive index sensor based on analyte filled defect hollow core bragg fiber.* IEEE Photonics Technology Letters, 2017, Vol. 29, 1391-1394.

[30] Y. Zhao, X. G. Li, L. Cai, and Y. N. Zhang, *Measurement of RI and temperature using composite interferometer with hollow-core fiber and photonic crystal fiber.* IEEE Transactions on Instrumentation and Measurement, 2016, Vol. 65, 2631-2635.

[31] J. Macomber, P. Lui, and R. Acuna, *Polymicro technologies fused silica capillary tubing: selecting a cutting method.* LCGC, The Application Notebook, 2009.

[32] *Introduction to spectroscopy and applications.* Ocean Optics.

[33] A. Z. Agnieszka, K. Elizaveta, and B. Akash, *3.06 - Biosensing, comprehensive nanoscience and nanotechnology (second edition).* Materials Science and Materials Engineering, 2019, Vol. 3, 105-126.

[34] S. Rutuja, B. P. Rajashri, and P. G. Pranit, *UV-Visible spectroscopy-a review.* International Journal of Institutional Pharmacy and Life Sciences, 2015, 490-505.

[35] S. Eaton-Magaa and B. Christopher, *An introduction to photoluminescence spectroscopy for diamond and its applications in gemology.* Gems Gemology, 2016, Vol. 52.

[36] S. B. Gurvinder and M. S. Rakesh, *Raman spectroscopy Basic principle, instrumentation and selected applications for the characterization of drugs of abuse.* Egyptian Journal of Forensic Sciences, 2015.

[37] D. Charu, P. Ishan, P. Himanshu, W. R. Pramod, C. P. Avinash, B. M. Shanti, and P. Sandip, *5.2 Fourier transform infrared spectroscopy,.* Nano- and Microscale Drug Delivery Systems, 2017, 147-164.

[38] A. B. Andrei, E. G. U, and Y. A. E. Hassan, *X-Ray diffraction: instrumentation and applications.* Critical Reviews in Analytical Chemistry, 2015, Vol. 45.

[39] T. Lu, *System and method for molecule sensing using evanescent light coupling approach*, U.S. Patent 9921164 B2, Mar. 20, 2018.

[40] K. Rahnavardy, V. Arya, A. Wang, and J. M. Weiss, *Investigation and application of the frustrated-total-internal-reflection phenomenon in optical fibers.* Appl. Opt, 1997, vol. 36, 2183-2187.

[41] D. G. OKeeffe, *Development of fiber optic evanescent-wave fluorescent-based sensors.* Doctoral, Dublin City University. School of Physical Sciences, 1995.

[42] S. Harlepp, J. Robert, N. Darnton, and D. Chatenay, *Subnanometric measurements of evanescent wave penetration depth using total internal reflection microscopy combined with fluorescent correlation spectroscopy.* Applied Physics Letters, 2004, Vol. 85, 3917-3919.

[43] A. Ghatak and K. Thyagarajan, *Introduction to fiber optics.* Cambridge University Press, 1997.

[44] K. Kawano and T. Kitoh, *Solving Maxwell's Equations and the Schrdinger Equation.* Introduction to Optical Waveguide Analysis, 2001.

[45] K. S. Nithin, *Hollow Fiber Coupler Sensor.* Masters Thesis, University of Victoria, 2018.

[46] Polymicro Technologies Polyimide coated fused silica capillary tubing, TSP320450 datasheet, 2016.

[47] N. Stankova, P. Atanasov, R. Nikov, R. G. Nikov, N. N. Nedyalkov, T. R. Stoyanchov, N. Fukata, K. Kole, E. Valova, J. Georgieva, and S. Armyanov, *Optical properties of polydimethylsiloxane (PDMS) during nanosecond laser processing.* Applied Surface Sciences, 2015, Vol. 374.

[48] *Sigma-Aldrich safety data sheet, 641928.* Sigma-Aldrich.

[49] *LabChem safety data sheet, LC154702.* LabChem.

[50] *Sigma-Aldrich safety data sheet, 755141-1G.* Sigma-Aldrich.

[51] H. Hellman, *Spectroscopy.* United States Atomic Energy Commission, 1968, Vol. 68-62126.

[52] C. N. Stedwell and N. C. Polfer, *Spectroscopy and the electromagnetic spectrum, laser photo dissociation and spectroscopy of mass-separated biomolecular ions. lecture notes in chemistry.* Springer, 2013, Vol. 83.

[53] T. H. Kauffmann, N. Kokanyan, and F. Marc, *Use of Stokes and anti-Stokes Raman scattering for new applications.* Journal of Raman Spectroscopy,, 2019.

[54] *Microscopy basics - resolution.* Nikon,, 2019.

[55] R. Lewandowska, *Raman microscopy: analysis of nanomaterials.* Encyclopedia of Materials: Science and Technology (Second Edition), 2010,1-6.

[56] M. James, F. Michael, K. Masanori, and C. Adam, *TEM study on the electrical discharge machined surface of single-crystal silicon.* Journal of Materials Processing Technology, 2013, Vol. 213, 801-809.

[57] *Microscope Objectives for Bioscience.* Nikon, 2019.

[58] X. Dong, G. Liu, J. Sun, J. Li, J. Liu, and G. Hong, *Preparation and properties of nanocrystalline Yb_2O_3.* Xiyou Jinshu Cailiao Yu Gongcheng/Rare Metal Materials and Engineering, 2001, Vol. 30, 73-76.

[59] P. Mukul, A. Kir'yanov, B. Sandip, S. Das, P. Mrinmay, S. Bhadra, M. Yoo, B. Alexander, and S. Jayanta, *Fabrication of large Core Yb_2O_3 doped phase separated Yttria-Alumino silicate nano-particles based optical fiber for use as fiber laser.* Rare Metal Materials and Engineering, 2012, Vol. 30, 73-76.

[60] Y. Jinqiu, C. Lei, H. Huaqiang, Y. Shihong, and H. H. W. Yunsheng, *Raman spectra of RE_2O_3 (RE=Eu, Gd, Dy, Ho, Er, Tm, Yb, Lu, Sc and Y): laser-excited luminescence and trace impurity analysis.* Journal of Rare Earths, 2014, Vol. 32, 1-4.

[61] U. Mustafa and A. Ozan, *Shortwave-infrared Raman spectroscopic classification of water fractions in articular cartilage ex vivo.* Journal of Biomedical Optics, 2016. Vol. 13.

[62] O. Takafumi, O. Noriko, Y. Taishi, A. J. F. Craig, K. Akihide, M. Hiroki, Y. Masato, K. Satoshi, and T. Masasuke, *Density functional study of the phase stability and Raman spectra of Yb_2O_3, Yb_2SiO_5 and $Yb_2Si_2O_7$ under pressure.* Physics Chemistry Chemical Physics, 2018. Vol. 24.

[63] D. P. Sugandha, K. Samanta, S. Jasveer, D. S. Nita, and A. K. Bandyopadhyay, *Anharmonic behavior and structural phase transition in Yb_2O_3.* AIP Advances, 2013. Vol. 3.

[64] T. Iliescu, S. Simon, D. Maniu, and I. Ardelean, *Raman spectroscopy of oxide glass system (1-x) $[Yb_2O_3.zLi_2O].xGd_2O_3$.* Journal of Molecular Structure, 1993. Vol. 294, 201-203.

[65] C. Jianlan and H. A. Gregory, *Raman and fluorescence spectroscopy of CeO_2, Er_2O_3,Nd_2O_3, Tm_2O_3, Yb_2O_3, La_2O_3, and Tb_4O_7).* Journal of Spectroscopy, 2015.

[66] A. Dalseth, S. Kristin, and K. H. Kari, *Hydrogen sulphide exposure in waste water treatment.* Journal of Occupational Medicine and Toxicology, 2018. Vol. 13.

[67] Z. Yu, D. B. Tyler, and X. Ming, *Hydrogen Sulfide (H_2S) releasing agents: chemistry and biological applications.* US National Library of Medicine National Institutes of Health, 2014 Vol. 15.

[68] L. Eunjung, M. Omar, S. W. Angela, and D. James, *Effect of environmental exposure to hydrogen sulfide on central nervous system and respiratory function: a systematic review of human studies.* International Journal Occupational Environmental Health, 2016 Vol. 22(1).

[69] L. M. R. Samantha, L. P. Linda, and P. Jim, *Environmental toxicology of hydrogen sulfide.* International Journal Occupational Environmental Health, 2017.

[70] H. Selene and J. Chou, *Hydrogen Sulfide: Human health aspects.* Agency for Toxic Substances and Disease Registry, World Health Organisation, 2003.

[71] K. Boris, *Raman investigation of H_2O molecule and hydroxyl groups in the channels of hemimorphite.* American Mineralogist, 2006, Vol. 91, 1355-1362.

[72] W. Dongqing, *An experimental study of the measurement of low concentration of hydrogen sulfide in aqueous solution.* Doctoral, University of Saskatchewan, 2006.

[73] X. C. Wu, W. J. Zhang, R. Sammynaiken, Q. H. Meng, D. Q. Wu, Q. Yang, W. Yang, E. M. Zhang, and R. Wang, *Measurement of low concentration and nano-quantity hydrogen sulfide in serum using unfunctionalized carbon nanotubes.* Measurement Science and Technology, 2009, Vol. 20.

[74] M. Monthioux, P. Serp, E. Flahaut, M. Razafinimanana, C. Laurent, A. Peigney, W. Bacsa, and J. Broto, *Introduction to Carbon Nanotubes.* Springer Handbook of Nanotechnology, 2010, 43-48.

[75] N. P. Valentin, *Carbon nanotubes: properties and application.* Materials Science and Engineering, 2004, 62-70.

[76] B. Ribeiro, E. Botelho, M. Costa, and C. Bandeira, *Carbon nanotube buckypaper reinforced polymer composites: A review.* Polmeros, 2017, Vol. 27.

[77] F. Wengu, K. Seokjoon, B. Eric, and V. Radisav, *Adsorption of Hydrogen Sulfide onto activated carbon fibers: effect of pore structure and surface chemistry.* American Chemical Society, 2005, Vol. 39, 9744-9749.

[78] H. Murphy, P. Papakonstantinou, and T. I. T. Okpalugo, *Raman study of multiwalled carbon nanotubes functionalized with oxygen groups.* American Vacuum Society, 2006.

[79] M. Zdrojek, W. Gebicki, C. Jastrzebski, T. Melin, and A. Huczko, *Studies of multiwall carbon nanotubes using Raman spectroscopy and atomic force microscopy.* Solid State Phenomena, 2004, Vol. 99, 265-268.

[80] T. Christian and R. Stephanie, *Raman scattering in Carbon nanotubes.* Light Scattering in Solid IX. Topics in Applied Physics,, 2007, Vol. 108, 171-172.

[81] R. Saito, M. Hofmann, G. Dresselhaus, A. Jorio, and M. S. Dresselhaus, *Raman spectroscopy of graphene and carbon nanotubes.* Journal Advances in Physics, 2010,413-550.

[82] P. Biagio and T. O. Robert, *Atomic absorption spectroscopy.* Journal of the American Oil Chemists Society, 1968, Vol. 45, Issue 11, 789792.

[83] S. Walter, *Atomic absorption spectroscopy: why has it become successful?.* Analytical Chemistry, 1991, 1033A-1038A.

[84] M. Yoji and M. Hiroshi, *Development of a low-loss optical circulator.* Furukawa Review, 2002, Vol. 22.

[85] P. D. John, *Distributed optical fiber sensors.* Distributed and Multiplexed Fiber Optic Sensors II, 1993.

[86] P. D. John, H. Kazuo, A. L. Robert, and A. M. Michael, *Optical fiber sensors.* Handbook of Optoelectronics: Enabling Technologies, 2017,Vol. 2, Chap.11.

[87] K. J. Siebert, *Relationship of particle size to light scattering.* Journal of the American Society of Brewing Chemists, 2018, Vol. 58(3), pp. 97-100.

[88] M. M. Gen, T. N. Mogileva, O. V. Aleksandr, D. L. Bulatov, and V. V. Vanyukov, *Nonlinear light scattering in a carbon nanotube suspension.* Quantum Electronics, 2010, Vol. 40.